2011

# Numerical analysis of a plasmoid thruster

Brittany Anne Dowell

## Recommended Citation

Dowell, Brittany Anne, "Numerical analysis of a plasmoid thruster" (2011). *Theses*. 429.
https://louis.uah.edu/uah-theses/429

# NUMERICAL ANALYSIS OF A PLASMOID THRUSTER

**by**

**BRITTANY ANNE DOWELL**

**A THESIS**

**Submitted in partial fulfillment of the requirements**
**for the degree of Master of Science in Engineering**
**in**
**The Department of Mechanical & Aerospace Engineering**
**to**
**The School of Graduate Studies**
**of**
**The University of Alabama in Huntsville**

**HUNTSVILLE, ALABAMA**
**2011**

In presenting this thesis in partial fulfillment of the requirements for a master's degree from The University of Alabama in Huntsville, I agree that the Library of this University shall make it freely available for inspection. I further agree that permission for extensive copying for scholarly purposes may be granted by my advisor or, in his/her absence, by the Chair of the Department or the Dean of the School of Graduate Studies. It is also understood that due recognition shall given to me and to The University of Alabama in Huntsville in any scholarly use which may be made of any material in this thesis.

Brittany A Dowell Jan 30, 2011
(student signature) (date)

# THESIS APPROVAL FORM

Submitted by Brittany Anne Dowell in partial fulfillment of the requirements for the degree of Master of Science in Engineering in Mechanical Engineering and accepted on behalf of the Faculty of the School of Graduate Studies by the thesis committee.

We, the undersigned members of the Graduate Faculty of The University of Alabama in Huntsville, certify that we have advised and/or supervised the candidate on the work described in this thesis. We further certify that we have reviewed the thesis manuscript and approve it in partial fulfillment of the requirements of the degree of Master of Science in Engineering in Mechanical Engineering.

1/23/11 Committee Chair
(Date)

Adam K. Martin 2/14/2011

____________________________________________

Robert A Frederick 2/14/11 Department Chair

02/23/11 College Dean

Rhonda Kay Gaede 4/18/11 Graduate Dean

# ABSTRACT

The School of Graduate Studies
The University of Alabama in Huntsville

Degree Master of Science in Engineering College/Dept. Engineering/Mechanical and Aerospace Engineering

Name of Candidate Brittany Anne Dowell

Title Numerical Analysis of a Plasmoid Thruster

The plasmoid thruster experiment (PTX) is a pulsed, inductive thruster developed at Marshall Space Flight Center and further tested at UAHuntsville Propulsion Research Center. The goal of this thesis is to numerically model PTX using MACH 2, a 2D magnetohydrodynamic code, to develop insights into the experiment. This thesis describes the numerical modeling, including the gas injection, circuit model, and plasmoid formation and acceleration. The numerical model showed plasmoid formation, and it was observed that the plasmoid decays on a short (~1 μs) time scale. Plasmoid translation downstream was not observed. The model also showed that the plasmoids remain intact longer when the gas has been preionized. Increased initial ionization also resulted in higher plasmoid velocities and densities. These observations are consistent with experimental observations. It was concluded that coupling between the plasmoid and the coil will be improved by increasing the initial ionization level.

Abstract Approval: Committee Chair

Department Chair Robert A Frederick 2/14/11

Graduate Dean Rhonda Kay Gaede 4/18/11

# ACKNOWLEDGMENTS

I would like to acknowledge and thank my committee members: Dr. Jason Cassibry, Dr. Adam Martin, Dr. Clark Hawk, and Dr. Robert Fredrick for their guidance and advice during this research and the compilation of this work. I would also like to thank the Propulsion Research Center for providing the funding for my graduate work.

# TABLE OF CONTENTS

Page

CHAPTER

# LIST OF FIGURES

Figure Page

# LIST OF TABLES

# LIST OF ABBREVIATIONS/ACRONYMS

| | |
|---|---|
| FARAD | Faraday Accelerator with Radio-Frequency Assisted Discharge |
| FIG | Fast Ionization Gauge |
| FRC | Field Reversed Configuration |
| ISRU | In-Situ Propellant Utilization |
| MACH | Multiblock Arbitrary Coordinate Hydromagnetic |
| MHD | Magnetohydrodynamic |
| MPD | Magnetoplasmadynamic |
| MSFC | Marshall Space Flight Center |
| PIT | Pulsed Inductive Thruster |
| PPT | Pulsed Plasma Thruster |
| PTX | Plasmoid Thruster Experiment |
| RLC | Resistive/Inductive/Capacitive |

# LIST OF SYMBOLS

| Symbol | Definition |
|---|---|
| $A$ | Area |
| $\vec{B}$ | Magnetic Field Vector |
| $C$ | Constant |
| $C_c$ | Coefficient in Anomalous Resistivity |
| $C_p$ | Specific Heat at Constant Pressure |
| $C_v$ | Specific Heat at Constant Volume |
| $c_{v_e}$ | Electron Specific Heat |
| $E$ | Energy |
| $\vec{E}$ | Electric Field |
| $e$ | Electron Charge |
| $F_g$ | Local Gravitational Force |
| $f$ | Coefficient in Anomalous Resistivity |
| $I$ | Total Current |
| $I_{sp}$ | Specific Impulse |
| $J$ | Current |
| $K$ | Boltzman Constant |
| $L$ | Inductance |
| $\vec{l}$ | Circuit Boundary |
| $\dot{m}$ | Mass Flow Rate |
| $m$ | Mass |

| | |
|---|---|
| $m_e$ | Electron Mass |
| $m_f$ | Final Mass |
| $m_o$ | Initial Mass |
| $m_{plenum}$ | Mass in the Plenum |
| n | Factor in Conservation of Mass Equation |
| $n_e$ | Electron Density |
| P | Momentum |
| p | Pressure |
| $P_e$ | Electron Thermal Pressure |
| Q | ‘Artificial’ Numerical Compressional Viscosity |
| R | Universal Gas Constant |
| R | Resistance |
| T | Thrust |
| T | Temperature |
| $T_e$ | Electron Temperature |
| $T_i$ | Ion Temperature |
| t | Time |
| r | Radius |
| $r_o$ | Impact Parameter |
| $r_{inlet}$ | Radius at the Inlet |
| $r_{wall}$ | Radius at the Wall |
| t | Time |
| $\vec{u}$ | Velocity Vector |

| | |
|---|---|
| $u_e$ | Exit Velocity |
| $u_{eq}$ | Equivalent Exit Velocity |
| $u_r$ | Radial Velocity |
| $u_z$ | Axial Velocity |
| $u_R$ | Radiation Energy Density |
| $\dot{v}$ | Acceleration of Rocket |
| $V$ | Volume |
| $V_c$ | Applied Voltage |
| $z$ | Axial Distance |
| $\chi_{ros}$ | Rosseland Mean Opacity |
| $\delta^{ji}$ | Kronecker Delta |
| $\Delta m$ | Change in Mass |
| $\Delta v$ | Change in Velocity |
| $\varepsilon_e$ | Electron Specific Internal Energy |
| $\varepsilon_o$ | Permittivity of Free Space |
| $\Phi_{eR}$ | Radiation Coupling |
| $\eta$ | Sum of Classical and Anomalous Electric Resistivities |
| $\eta_S$ | Spitzer Resistivity |
| $\kappa_e$ | Electron Thermal Conductivity |
| $\ln \Lambda$ | Coulomb Logarithm |
| $\lambda_D$ | Debye Length |
| $\mu$ | Shear Modulus |
| $\mu_o$ | Permeability of Free Space |

| | |
|---|---|
| $\nu_{de}$ | Electron Drift Velocity |
| $\nu_s$ | Ion Sound Speed |
| $\omega_{pi}$ | Ion Plasma Frequency |
| $\theta$ | Coil Half Angle |
| $\rho$ | Density |
| $\sigma^{d_{ij}}$ | Elastic Stress-Deviators |
| $\tau_{ei}$ | Electron-Ion Equilibration Time |

*Dedicated to my loving grandma, Margaret Anne Calvert.*

# CHAPTER I

# INTRODUCTION

For deep space missions beyond Mars, propulsion systems with high specific impulses ($I_{sp}$) beyond the reach of chemical propulsion are desirable in order to reduce trip times and increase the payload mass fraction. Most in-space propulsion approaches require thermal expansion of a gas out of a nozzle, which is limited by the chemical potential energy released in combustion processes. Higher exhaust velocities are desired for many types of missions, and this can be accomplished via direct acceleration of charged particles via electromagnetic body forces using electric propulsion systems [1]. Electric propulsion is a candidate approach which achieves high exhaust velocities [2] by means of direct "acceleration of gases for propulsion by electrical heating and/or by electric and magnetic body forces" [1]. Electric propulsion systems can reduce the weight of propellant for a given $\Delta V$ and can increase the dry/wet mass ratio of the vehicle. However, electric thrusters need power supplies and power conditioning systems that add to the weight of the overall propulsion system.

One such electromagnetic thruster is the plasmoid thruster, a kind of pulsed inductive thruster. This system has potential as a high thrust, high exhaust velocity propulsion which enables some deep space missions. The Plasmoid Thruster Experiment (PTX) [3] was an experiment to investigate certain aspects of plasmoid thrusters. This thesis models certain aspects of PTX, to help in understanding the coupling between the propellant and propulsive processes. In the next couple of sections, some of the characteristics of electric propulsion systems will be described.

## 1.1 Benefits of Electric Propulsion

There are a few figures of merit that are important when considering space missions: thrust (T), specific impulse ($I_{sp}$), and the payload mass fraction. The derivations are based on the development of the rocket equation, for which the sources are numerous [4]. The equation of motion for a simple rocket in a gravitational field is

$$m\dot{v} = \dot{m}u_{eq} + F_g . \tag{1.1}$$

where m is the mass of the vehicle, $\dot{v}$ is the acceleration of the rocket, $F_g$ is the local gravitational force , and $u_{eq}$ is the equivalent exit velocity relative to the rocket,

$$u_{eq} = u_e + \frac{(p_e - p_0) * A_{exit}}{\dot{m}} .$$

It is assumed that the pressure at the exit, $p_e$, is approximately equal to the freestream pressure, $p_o$. The first term on the right is the thrust of the rocket,

$$T = \dot{m}u_e . \tag{1.2}$$

If it is assumed that the exhaust velocity remains constant, and the local gravitational field is negligible when compared to the thrust, or if it exhausts its propellant over a short period of time, the change in velocity is given by

$$\Delta v = u_e \ln \frac{m_o}{m_f} , \tag{1.3}$$

where the final mass ($m_f$) is the propellant mass expelled to achieve the Δv subtracted from the initial mass

$$m_f = m_o - \Delta m . \tag{1.4}$$

Equation (1.3) can be rearranged to give the inverse of the vehicle mass fraction $m_o/m_f$ as given by the rocket equation

$$\frac{m_f}{m_o} = e^{-\Delta v/u_e} . \tag{1.5}$$

As shown in equation (1.5), for a given mission Δv, a higher exhaust velocity will give a higher mass fraction.

Electric propulsion systems are generally power limited as opposed to chemical propulsion, which is limited by the amount of energy that can be expended from a chemical reaction. Existing practical chemical propulsion systems have a maximum $I_{sp}$ of 450 seconds, while electric propulsions systems have the potential to exceed $I_{sp}$'s of over 10,000 seconds [1]. Applications of electric propulsion include, but are not limited to attitude control, station keeping, orbital adjustment and transfer, formation flying, and interplanetary missions.

There are three types of electric propulsion: electrothermal, electrostatic, and electromagnetic. Electrothermal thrusters, such as arcjets and resistojets, heat a gas electrically, and then expand the gas through a nozzle. It is generally characterized by higher thrust and lower $I_{sp}$ relative to the other electric propulsion systems. The exhaust velocity scales with the square root of temperature per molecular weight of the propellant, and thus electrothermal propulsion is susceptible to the same thermal limitations that prevent high exhaust velocities in chemical propulsion. Electrostatic thrusters, such as ion and colloid thrusters, accelerate the propellant by direct application of electric body forces to ionized particles. These thrusters are limited by the amount of voltage applied to the system, and are space-charge limited. They are characterized by low thrust and high $I_{sp}$. Electromagnetic thrusters include magnetoplasmadynamic (MPD) thrusters, pulsed inductive thrusters (PIT), and plasmoid thrusters. They will be discussed in the next section.

## 1.2 Electromagnetic Propulsion

Electromagnetic thrusters use internal and external magnetic fields with electric currents to accelerate an ionized propellant stream. This propellant stream can be quasi-neutral (have no net macroscopic space-charge), and thus these thrusters do not have the space-charge limitations to which electrostatic thrusters are subject. Electromagnetic thrusters can be steady-state or pulsed, and directly or inductively coupled. Steady-state thrusters will have current density patterns, flow velocities, and magnetic fields that remain constant in time at every point, and are usually directly coupled systems. Pulsed systems will undergo vigorous pulsations in time [1]. There are directly and indirectly coupled electromagnetic propulsion systems. Directly coupled systems have electrodes that are in direct contact with the gas. Because of the high voltage breakdown initiation, high current electron emission, ion bombardment flux, thermal conduction, and radiative transport, electrode damage occurs [1, 5]. Inductively coupled systems will be discussed in the next section.

### 1.2.1 Inductively Coupled Plasma Propulsion

In inductively coupled systems, the interaction between an induced secondary current and the magnetic field from a primary coil produce the Lorentz force, or J x B force to accelerate the plasma. Because the gas is not in direct contact with the electrodes, electrode erosion is significantly reduced. Inductively coupled thrusters, by their nature, are pulsed devices. They generally consist of 3 elements: a drive coil to accelerate the plasma, a capacitor to store energy for the pulse, and a switch to close the circuit [6]. Some common inductively coupled thrusters are the Pulsed Inductive Thruster (PIT) [1], the Faraday Accelerator with Radio-frequency Assisted Discharge (FARAD) [7], and the conical theta-pinch [1].

There are a variety of loss mechanisms in accelerating the plasma, including ionization losses, heating of the propellant, radiation, and the coupling efficiency between the coil and the plasma [6]. Numerical studies indicate that for ground tests (the only kind so far conducted) as the vacuum chamber walls are moved inward, the overall inductance of the coil is lowered and the electromagnetic acceleration of the plasma is reduced [8]. This characteristic results in experimental data that likely underestimates the actual in-space performance of the thruster.

The plasmoid thruster is a pulsed, inductive, electromagnetic device that uses the Lorentz force to accelerate plasmoids, generating thrust. There are several promising features of this thruster. The plasmoid thruster experiment (PTX) has demonstrated exhaust velocities corresponding to $I_{sp}$'s of up to 4600s [3]. In inductively coupled systems, the interaction between an induced secondary current and the magnetic field from a primary coil produce the Lorentz force, or J x B force to accelerate the plasma. Since the gas is not in direct contact with the electrodes, electrode erosion should be significantly reduced. In the next chapter we discuss the PTX experiment.

# CHAPTER II

# PLASMOID THRUSTER EXPERIMENT

There are several promising characteristics of the plasmoid thruster. As previously mentioned, this thruster does not have the issues of space-charge limitation, magnetic detachment, and has reduced electrode erosion compared to that which occurs in other thrusters. The plasmoid thruster, like other pulsed inductive thrusters, can use a variety of propellants including ammonia, hydrogen, and argon. This makes this thruster ideal for missions such as In-Situ Propellant Utilization (ISRU).

A plasmoid (also known as a compact toroid) is a compact plasma with an internal magnetic field structure [9]. If the compact toroid has only poloidal magnetic field and toroidal current, it is referred to as a Field Reversed Configuration (FRC). If it has both poloidal and toroidal magnetic fields and currents, it is called a spheromak.

The plasmoid thruster experiment (PTX) was constructed at Marshall Space Flight Center (MSFC) [3]. The plasmoid thruster is a pulsed, inductive electromagnetic device that uses the Lorentz force to accelerate plasmoids, generating thrust. A schematic of the plasmoid thruster can be seen in Figure 2.1.

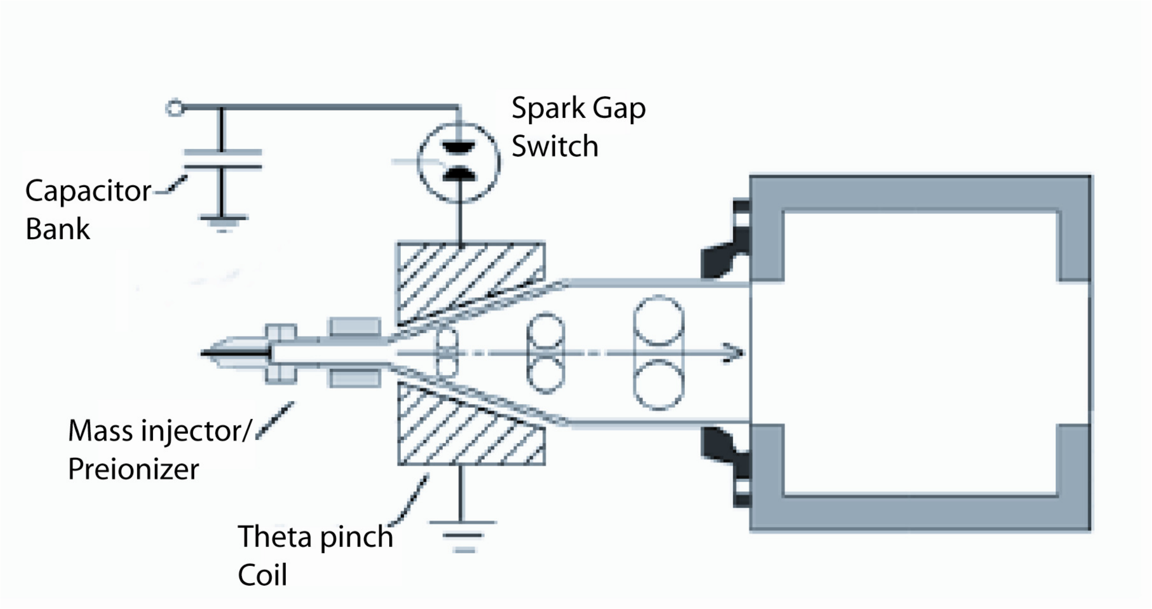

Figure 2.1 Plasmoid Thruster Schematic (Reproduced from Reference [3])

## 2.1 Gas Injection

Gas (Ar and $H_2$ were used during the experiment) is pressurized inside a plenum of volume upstream of the solenoid valve. Once the valve opens, the gas is released expanding down a 2.6 mm radius, 184 mm long Pyrex tube and subsequently inside the $17.5^{o}$ half-angle, single turn θ-pinch coil, shown in Figure 2.2. To measure the amount of gas injected into the system, a fast ionization gauge (FIG) was set up at the exit of the coil ($z = 0$ mm), at $z = -30$mm, and at $z = 60$mm. The FIG measured the pressure that passed by the gauge over time.

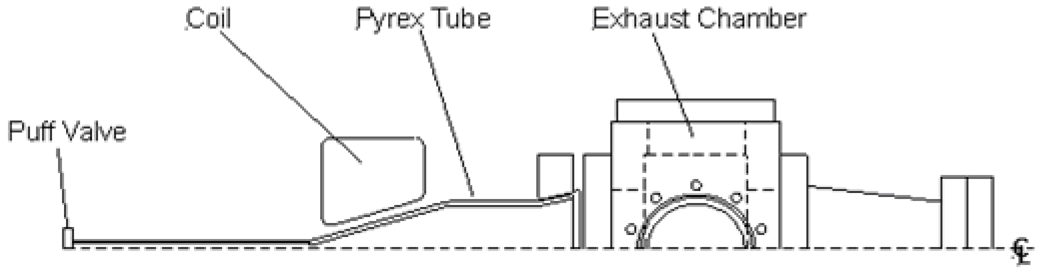

Figure 2.2 Half Plan View of PTX

## 2.2 Plasmoid Formation

Gas is puffed into the Pyrex tube by a solenoid valve. An optical trigger signal is then sent to the high-voltage pulser triggering the spark-gap switch. The spark gap closes, allowing the capacitor bank to discharge through the coil. The time between when the gas is puffed and when the bank is fired is called the puff valve delay time, $t_{puff}$.

The θ-pinch is then driven by a 560 nF, 40 kV capacitor bank discharged through a spark-gap switch. The current in the rings sinusoidally. When the coil is fired, the rapidly changing axial magnetic field creates an azimuthal electric field which breaks down the gas. At the same time, a bias magnetic field is embedded into the ionized gas. Once the gas is fully ionized, the flux is frozen in the plasma. The current in the coil then reverses direction, producing anti-parallel magnetic field lines. The field lines will compress, tear, and reconnect, forming a field reversed configuration (FRC). A large azimuthal current (**J**) is induced in the plasma by the magnetic field (**B**). The Lorentz, or **JxB**, force accelerates the plasma away from the coil, generating thrust. This process is shown in Figure 2.3.

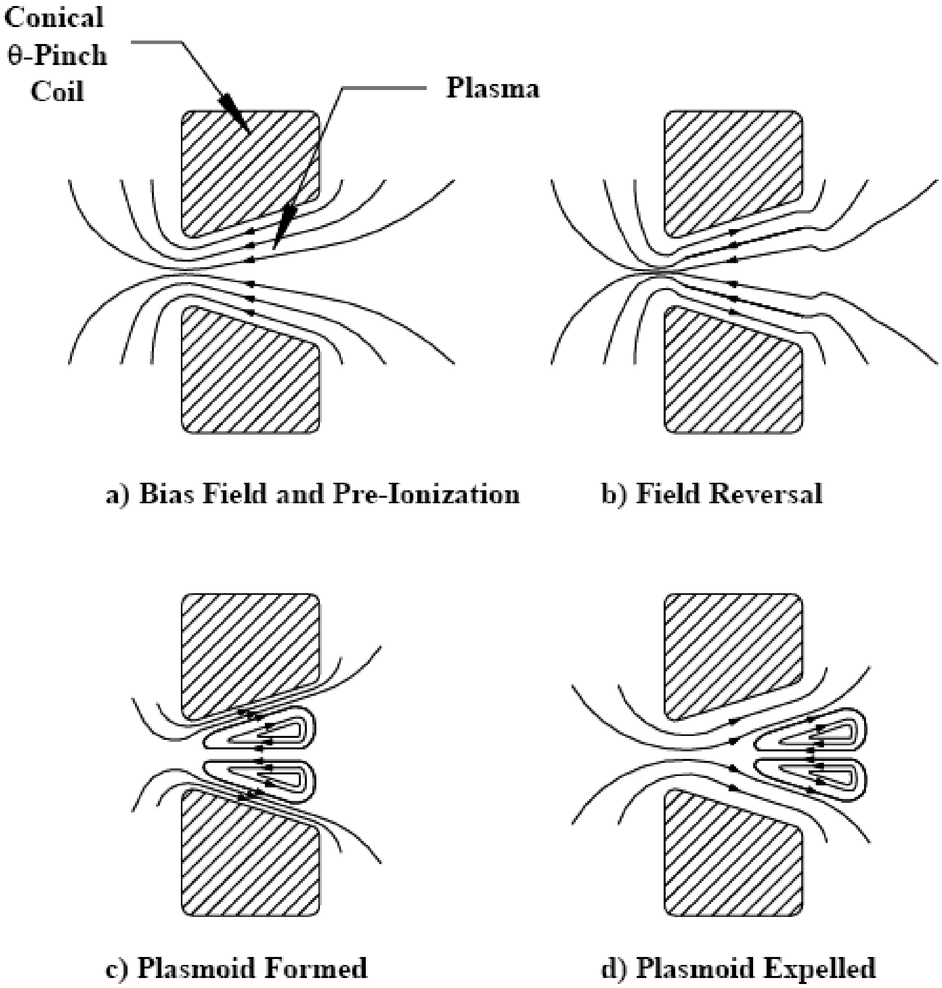

Figure 2.3 Plasmoid Formation

## 2.3 Objective

The objective of this thesis is to develop a model to simulate PTX at least qualitatively and to develop insights into how the coil couples to the plasma.

In Chapter 3, the numerical model will be discussed. Chapter 4 will cover the results of the simulations. Chapter 5 will cover the conclusions and will recommend future work.

# CHAPTER III

# NUMERICAL MODEL

There are four distinct problems in modeling the plasmoid thruster that must be considered separately: the gas injection, circuit dynamics, plasmoid formation, and plasmoid acceleration/translation. The gas injection phase is a purely hydrodynamic process which occurs over a time scale of ~10 ms, and includes the valve, Pyrex tube, and coil geometry. When the circuit fires, the energy is discharged through the coils and dissipated in the circuit over a period of ~20 μs. Resistive/inductive/capacitive (RLC) circuits usually consist of a coupled set of ordinary differential equations relating the voltage and current as a function of time. Formation and acceleration of the plasmoid require magnetohydrodynamic equations of motion along with an equation of state and transport coefficient models (resistivity and thermal conduction) appropriate for a magnetized plasma. Since formation and acceleration involve very similar physical processes the same model can largely be used for both. The three distinct models are discussed below, in the context of the physical process, and are labeled ‘gas injection’, ‘circuit’, and ‘plasmoid’. Since the gas dynamics and magnetohydrodynamics modeling from the coil volume to the translation section use the same numerical code, we will precede the description of the models with one of the code.

## 3.1 Two-Dimensional Numerical Code

The Multiblock Arbitrary Coordinate Hydromagnetic (MACH) codes are a family of complex geometry magnetohydrodynamic (MHD) codes. MACH was developed by the

Center for Plasma Theory and Computation at the Air Force Research Laboratory: Phillips Research Site and its prime contractor, NumerEx [10]. It uses a multiblock structure with arbitrarily shaped hexahedral cells. Spatial derivatives are done using a finite volume method. It is an Arbitrary Lagrangian-Eulerian code, which allows it to be run in an Eulerian (grid at rest in laboratory frame) or Lagrangian frame (grid at rest in the fluid frame). MACH2 is a 2 ½-D code – it includes all 3 spatial vector fields, but sets the spatial derivative to zero for the vector orthogonal to the 2-D plane specified. This model is in the r-z plane, so the derivative of the θ–direction will be set to zero. The equations of MACH are as follows:

<u>Mass Continuity</u>

$$\frac{\partial\rho}{\partial t} = -\nabla\bullet\left(\rho\vec{u}\right) \tag{3.1}$$

<u>Fluid Momentum</u>

$$\rho\frac{\partial u^i}{dt} = -\rho u^j\nabla_j u^i + \nabla_j\left[-\left(P+Q+\frac{1}{3}u_R\right)\delta^{ji} + \frac{1}{\mu_o}\left(B^j B^i - \frac{1}{2}B^2\delta^{ji}\right) + \sigma^{d_{ji}}\right] \tag{3.2}$$

<u>Electron Specific Internal Energy</u>

$$\rho\frac{\partial\varepsilon_e}{dt} = -\rho\vec{u}\bullet\nabla\varepsilon_e - P_e\delta^{ji}\nabla_i u_j + \eta J^2 - \vec{J}\bullet\left(\frac{\nabla P_e}{en_e}\right) + \nabla\bullet\left(\kappa_e\nabla T_e\right) - \Phi_{eR} - \rho c_{v_e}\frac{\left(T_e - T_i\right)}{\tau_{ei}} \tag{3.3}$$

<u>Ion Specific Internal Energy</u>

$$\rho\frac{\partial\varepsilon_i}{dt} = -\rho\vec{u}\bullet\nabla\varepsilon_i + \left[-\left(P_i+Q\right)\delta^{ji} + \sigma^{d_{ji}}\right]\nabla_i u_j + \nabla\bullet\left(\kappa_i\nabla T_i\right) + \rho c_{v_e}\frac{\left(T_e - T_i\right)}{\tau_{ei}} \tag{3.4}$$

Radiation Energy Density

$$\frac{\partial u_R}{\partial t} = -\rho\vec{u} \bullet \nabla u_R - \frac{4}{3} u_R \nabla \bullet \vec{u} + \nabla \bullet \left(\rho \chi_{ros} \nabla u_R\right) + \Phi_{eR} \tag{3.5}$$

Magnetic Induction

$$\frac{\partial \vec{B}}{\partial t} = \nabla \times \left(\vec{u} \times \vec{B}\right) - \nabla \times \left(\eta \vec{J}\right) - \Delta \times \left(\frac{\vec{J} \times \vec{B}}{en_e}\right) + \nabla \times \left(\frac{\nabla P_e}{en_e}\right) \tag{3.6}$$

## 3.2 Gas Injection Model

To capture the physics of the plasmoid, it is necessary to specify the initial conditions of the gas inside the coil volume. The initial conditions depend on the dynamic process of the puff valve evacuation, propagation of the gas down the Pyrex tube, and expansion of the gas inside the coil volume.

Detailed knowledge of the initial density and temperature of pressure distribution would be desirable, but experiments to date have had only limited measurements of the pressure at three points downstream of the inlet of the coil. These measurements were taken with a fast ionization gauge and posed a challenge to approximating the initial conditions. First, the ionization gauges were used at pressures that pushed the limits for which they were designed. Second, since there was only one thermodynamic property measured at three positions, the state of the gas could not be determined. In summary, only a qualitative pressure profile was known at three positions.

Several options were explored to simulate the gas puff while being consistent with this limited pressure data. In all cases, the basic approach was to come up with a model to determine time dependent flow conditions for the inlet to the coil, and these conditions would be used as boundary conditions for MACH2. Then MACH2 was run and pressure measurements were compared with experimental data. For completeness, all of the approaches tried will be discussed.

MACH2 was initially considered for the valve evacuation and gas propagation in the Pyrex tube. This was rejected for two primary reasons. First, the solenoid valve has a finite opening and closing time, excessively complicating the model. Second, the orifice between the valve and the Pyrex tube was a fraction of a millimeter, requiring an intolerably high grid resolution in terms of available computational resources.

The next option considered was to use fully developed viscous flow. For this, several assumptions were made. It was assumed that 95% of the gas in the plenum is evacuated in the time the FIG measurements were taken. It was also assumed that by the time the gas reached the inlet of the coil, the flow was isothermal, and that there is no acceleration in the z- or θ- directions. The fully developed viscous momentum equation is

$$u_r \frac{\partial u_z}{\partial r} + u_z \frac{\partial u_z}{\partial z} = \frac{1}{\rho}\frac{dp}{dz} - \frac{\mu}{\rho}\left[\frac{1}{r}\frac{\partial}{\partial r}\left(r\frac{\partial u_z}{\partial r}\right) + \frac{\partial^2 u_z}{\partial z^2}\right]. \tag{3.8}$$

This then reduces to

$$\frac{1}{\rho}\frac{dp}{dz} = \frac{\mu}{\rho}\left[\frac{1}{r}\frac{\partial u_z}{\partial r} + \frac{\partial^2 u_z}{\partial r^2}\right], \tag{3.9}$$

which has the solution

$$u(r) = \frac{C}{4}\left(r_{wall}^2 - r^2\right), \tag{3.10}$$

where

$$C = \frac{1}{\mu}\frac{dp}{dz}. \tag{3.11}$$

This can then be averaged across the radial area to get the average radial velocity

$$u = \frac{1}{\pi r_{wall}^2} \int_0^r 2\pi r u(r) dr \tag{3.12}$$

to get

$$u = \frac{C r_{wall}^2}{8}. \tag{3.13}$$

The temperature is then iterated until the conservation of mass is satisfied

$$95\% m_{plenum} = \int_{t_o}^{t_f} \dot{m} dt = \int_{t_o}^{t_f} \left(\rho A u\right)_{inlet} dt. \tag{3.14}$$

The temperature that satisfied the conservation of mass was 30K. When this was input into the model, the pressures at the points where the FIG measurements were taken were much lower than those of the experimental data.

Another technique examined assumed subsonic velocity through the coil. It was also assumed that the gas had thermally expanded before reaching the inlet of the coil. This means the velocity and mass flow rate can be assumed to be constant through the coil

$$\left(\rho A u\right)_1 = \left(\rho A u\right)_2, \tag{3.15}$$

where 1 and 2 are arbitrary points along the coil. If point 1 is known,

$$\rho(z) = \frac{\rho_1 A_1}{A(z)}. \tag{3.16}$$

The ideal gas law states

$$p = \rho R T. \tag{3.17}$$

The pressure can then be found as a function of z-position, assuming a constant temperature.

$$\frac{dp}{dz} = \frac{d\rho}{dz}RT = -RT\frac{\rho_1 A_1}{\left[A(z)\right]^2}\frac{dA(z)}{dz}, \qquad (3.18)$$

where the area is that of a circle with a radius of

$$r = r_{inlet} + z\tan\theta \qquad (3.19)$$

and θ is the coil half angle.

Equation (3.18) was numerically integrated to find $\frac{dp}{dz}$ to input into the viscous equations above. This technique did not satisfy the conservation of mass (3.14).

Finally, it was decided to use the experimental data along with the conservation of mass and energy equations to find a transient density profile using a constant velocity and temperature. Again, it is assumed that 95% of the gas inside the plenum is evacuated in the time the experimental data was taken. It is also assumed that the density at the inlet follows that of the density downstream, and only differs by a factor *n*. That is,

$$\rho_{inlet} = n\rho_{z=-30mm} = n\frac{p_{z=-30mm}}{RT}. \qquad (3.20)$$

Since the temperature is assumed to be constant throughout the coil, *R* and *T* can be absorbed into the constant *n*, making

$$\rho_{inlet} = np_{z=-30mm}. \qquad (3.21)$$

The conservation of mass is then

$$.95\rho_{plenum}V_{plenum} = \int (\rho A u)_{inlet}\, dt. \qquad (3.22)$$

To satisfy the energy equation, the internal energy of the plenum before the gas puff valve is opened must be equal to the energy of the gas that passes the inlet. The internal energy in the plenum is

$$E_{plenum} = m_{plenum} C_v T_{plenum} \tag{3.23}$$

and the energy of the expanding gas is

$$E_{plenum} = \int \dot{m} \left( C_p T + \frac{u^2}{2} \right) dt , \tag{3.24}$$

where

$$\dot{m} = \rho_{inlet} A u \tag{3.25}$$

and the gas constants are those for diatomic molecules

$$\begin{gathered} C_v = \frac{5}{2} R \\ C_p = \frac{7}{2} R \end{gathered} . \tag{3.26}$$

Equations (3.22) and (3.24) can be combined to find the constant n and the velocity u for the gas injection model.

## 3.3 Circuit Model

PTX used a tank (LC) circuit that rings sinusoidally [3]. The circuit parameters of the experiment include 560 nF capacitance, 122nH external inductance, 35nH coil inductance, 60 m\Ohm external resistance, and a charge voltage of 35kV.

MACH2 has a routine to calculate the current in a RLC circuit given the aforementioned parameters. The equation it solves is as follows:

$$V_c(t) - I(t)R - \dot{I}(t)L - \int \vec{E} \bullet d\vec{l}_{CircuitBoundary} = 0\,. \tag{3.27}$$

## 3.4 Physical Conditions

Two important parameters that must be specified to accurately model the physics of a system using MACH2 are the resistivity model and the equation of state model. An accurate geometry of the experiment must also be specified.

### 3.4.1 Geometry

The geometry of PTX was modeled using MACH2. The geometry modeled begins at the inlet to the coil and encompasses the translation section downstream, as well as the vacuum chamber, as seen in Figure 3.1. It is assumed to be radially symmetric about the y-axis shown below. This geometry will be sufficient to see the formation of the plasmoid as well as its translation.

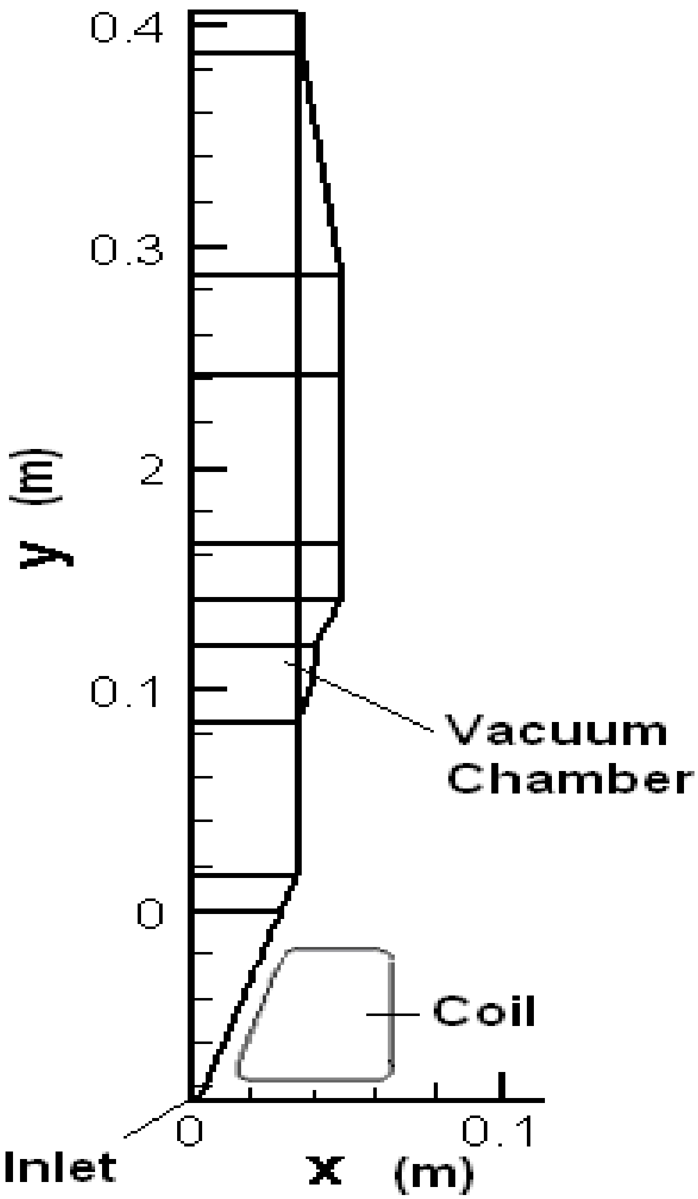

Figure 3.1 Model Geometry

### 3.4.2 Resistivity Model

Resistivity is the measure of how much a material opposes the flow of electric current. There are two types of resistivities important to plasmoid formations: classical and anomalous resistivity. In classical resistivity, the Joule heating goes predominantly to the electrons, and occurs when the magnetic field dissipation is dominated by electron-ion scattering collisions. This model is frequently called 'Spitzer' resistivity given by [3]

$$\eta = \frac{\pi e^2 m^{1/2}}{(4\pi\varepsilon_o)^2 (KT_e)^{3/2}} \ln\Lambda, \tag{3.28}$$

where

$$\Lambda = \lambda_D r_o = 12\pi n \lambda_D^3. \tag{3.29}$$

The anomalous resistivity used is the Chodura resistivity. This anomalous resistivity is believed to arise from current driven microinstabilities that occur when the electron drift velocity is greater than the ion thermal speed [12]. The anomalous resistivity can be expressed as

$$\eta_{an} = \frac{m_e \upsilon_{an}}{ne^2}, \tag{3.30}$$

$$\upsilon_{an} = C_c \omega_{pi} \left[ 1 - e^{-\left| \upsilon_{de} / f\upsilon_s \right|} \right], \tag{3.31}$$

where $\upsilon_s$ is the ion sound speed and $\omega_{pi}$ is the ion plasma frequency. The coefficients $C_c$ and f were set to 0.1 and 3 respectively, which was found to yield good agreement with experimental data with other FRC experiments [12].

### 3.4.3 Equation of State Model

The equation of state model used for this instance is the ideal gas equation of state. This is the simplest model. It uses an adiabatic $\gamma$–law. The pressure, electron temperature, and ion temperatures are calculated once a ratio of specific heat, atomic number, and atomic weight of the gas is specified.

## 3.5 Scope of Study

This model is a simulation of the PTX experiments done at MSFC. The motivation for the study was to see if insights into the coupling between the coil and the plasma could be observed. Hydrogen was used as the working fluid, and the gas injection model is based on experimental data corresponding to a plenum pressure of 10 psig. This pressure was chosen such that the fast ionization gauges would not become saturated. These conditions resulted in the highest exhaust velocities values seen during the Plasma Thruster Experiment [3].

# CHAPTER IV

# RESULTS

## 4.1 Gas Injection

As shown in Section 3.2, the velocity and coefficient for density were calculated for various temperatures and are shown in Table 4.1. A temperature of 150K was selected as the inlet temperature for the gas injection model.

Table 4.1 Gas Injection Parameters

| Temperature (K) | Constant n ($kg/m^3/Pa$) | Velocity u (km/s) |
|---|---|---|
| 50 | 8.36 E -7 | 7.603 |
| 100 | 8.47 E -7 | 7.508 |
| 150 | 8.58 E -7 | 7.411 |
| 200 | 8.69 E -7 | 7.313 |
| 273 | 8.87 E -7 | 7.168 |

The constant, n, was multiplied by the time-dependent experimental pressure measurement at z = -30mm to give the density at the inlet. There is only a 6% difference between the values of n and u at 50K and 273K, so a slightly different inlet temperature will not greatly impact the gas injection model.

## 4.2 Circuit Model

A plot of the currents calculated by MACH2 and measured experimentally is shown in Figure 4.1. The 1.7 μs delay between the signal sent to the spark-gap switch and the coil firing can be seen in the figure. The current measured in the experiment peaks at 52.5 kA. MACH2 calculates the first peak to be at approximately 56.5 kA, which is 7.6% higher than the experimental result [3]. At the second peak, the MACH2 current is only 1% higher than that of the experimental measurements.

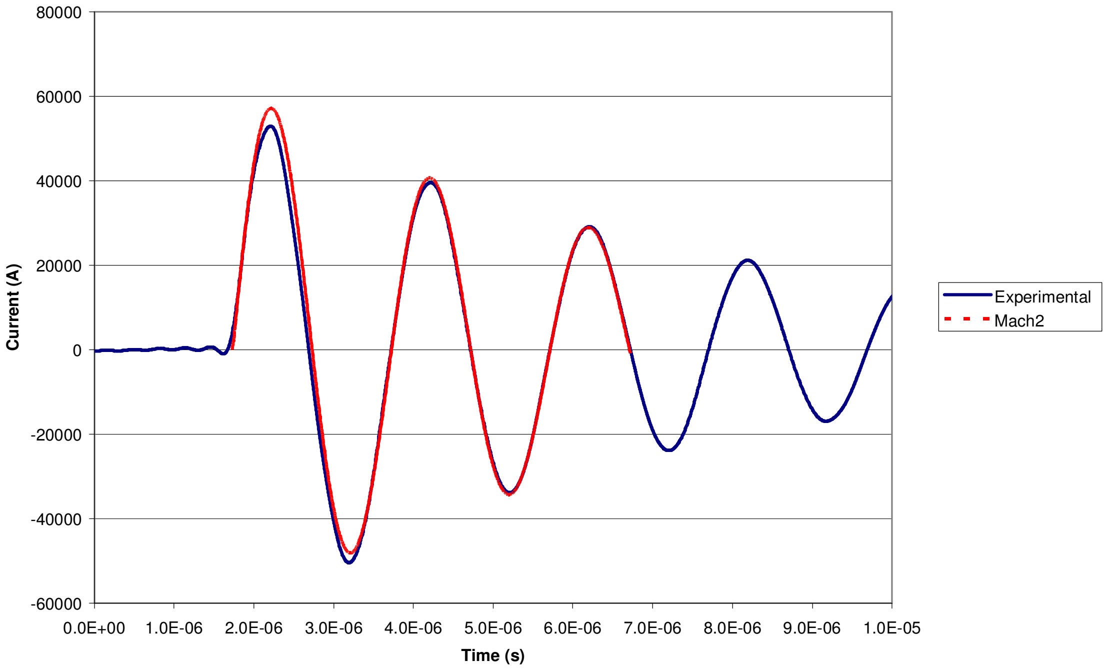

Figure 4.1 Bank Current Probe 1 Comparison

## 4.3 MACH2 Model

There were three experimental diagnostics for comparison with the numerical model: external $B_z$ probes, internal $B_z$ probes, and downstream interferometry measurements. These will be discussed in this section.

### 4.3.1 External Magnetic Field Measurements

Three external $B_z$ probes were placed between the θ-pinch coil and the Pyrex tube in which the plasmoids are formed. The placement of these probes is outside the computational mesh of the numerical model. However, a comparison was made between the experimental $B_z$ probes and virtual $B_z$ probes at the same z-positions at the outer portion of the domain. Table 4.2 shows the positions of the probes.

Table 4.2 External Probe Locations

| | Experimental | | MACH2 | |
|---|---|---|---|---|
| | r (m) | z (m) | r (m) | z (m) |
| Probe 1 | 0.01285 | -0.06743 | 0.00814 | -0.06743 |
| Probe 2 | 0.02241 | -0.0371 | 0.017703 | -0.0371 |
| Probe3 | 0.02996 | -0.01316 | 0.025251 | -0.01316 |

Although the radii of the probe positions differ, the magnetic field measurements at these z-positions are very similar, as shown in Figures 4.2 through 4.4.

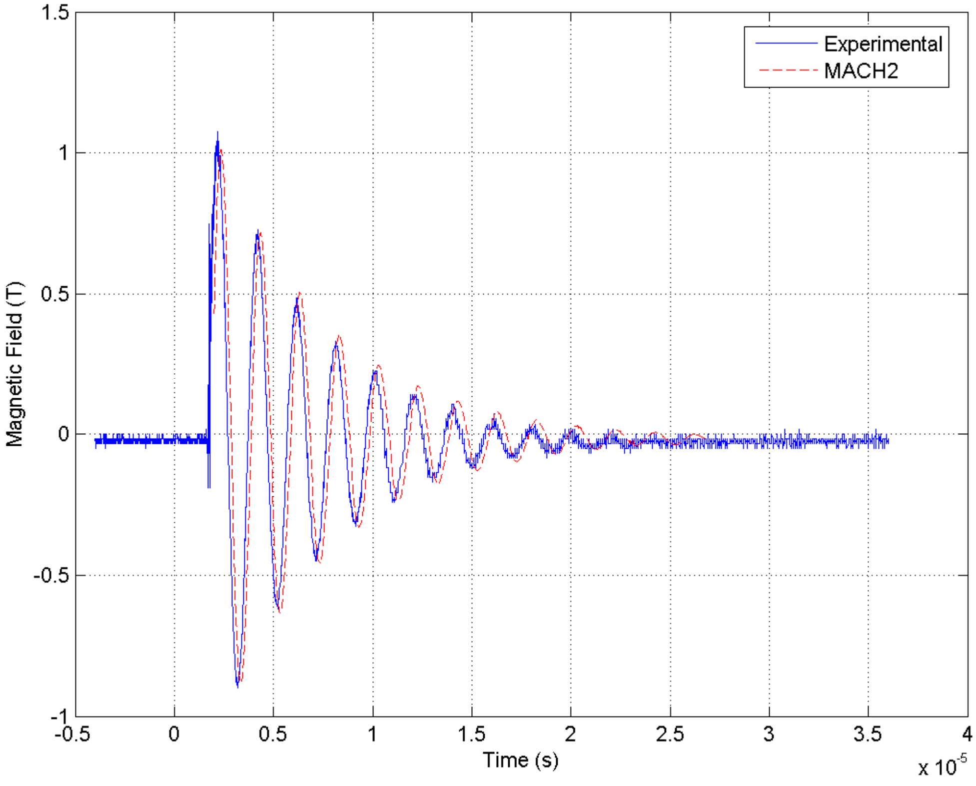

Figure 4.2 External $B_z$ Probe 1

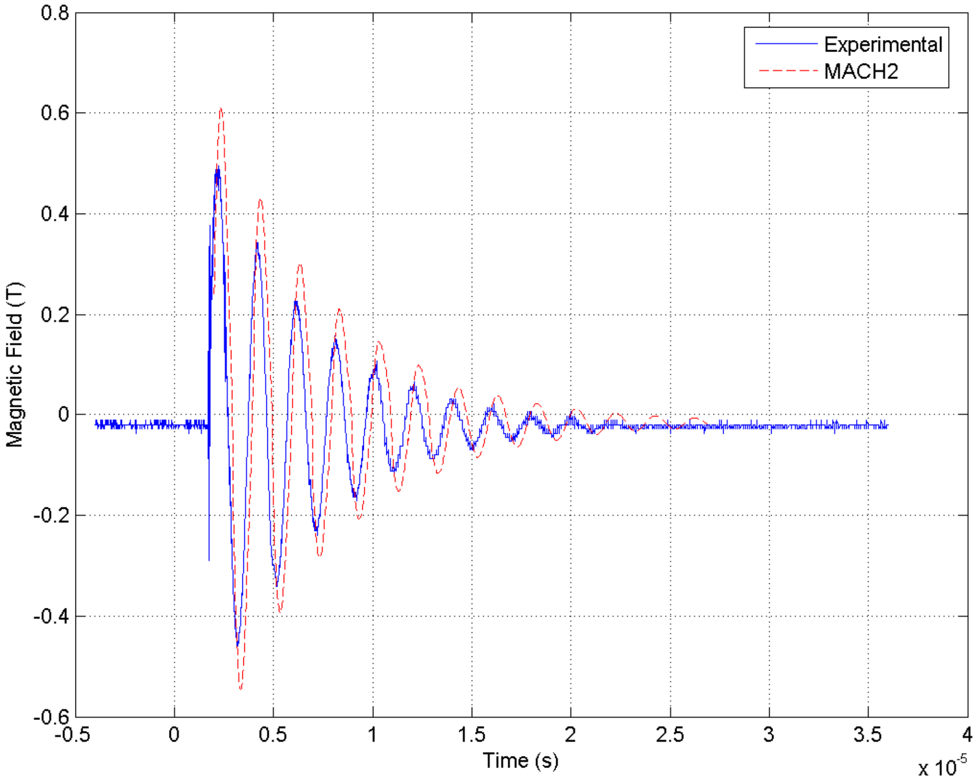

Figure 4.3 External $B_z$ Probe 2

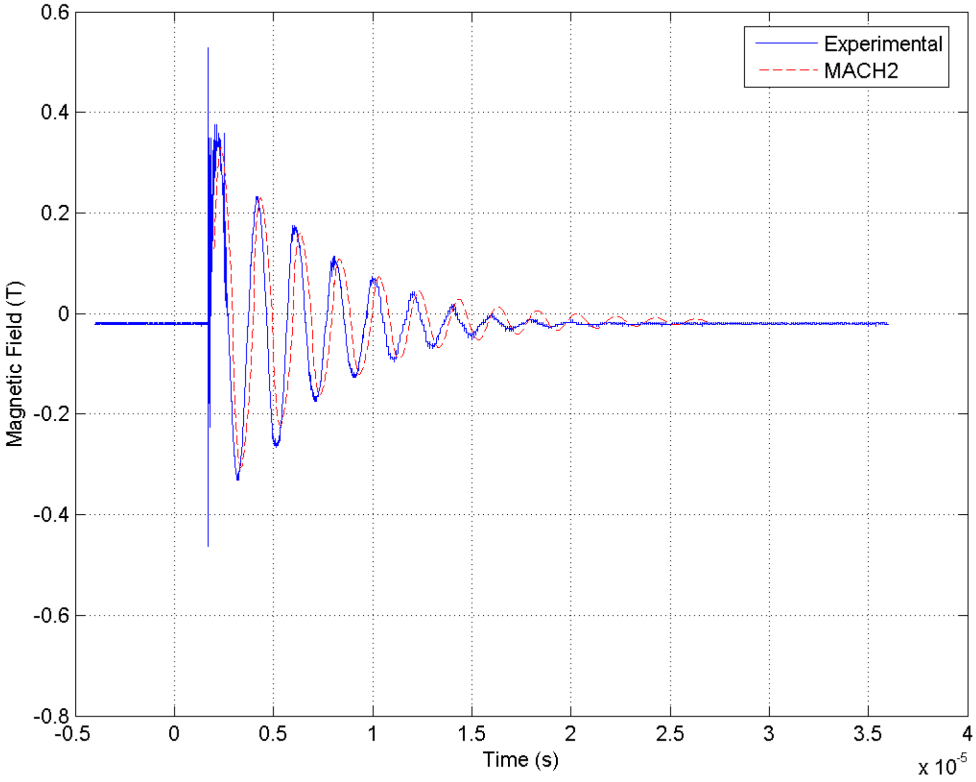

Figure 4.4 External $B_z$ Probe 3

The magnetic field measurements are within 1.5% of each other for both probes 1 and 3 when measured at the first peak. Probe 2 has a more significant deviation between the experimental and virtual probe measurements.

### 4.3.2 Internal Probe Measurements

Experimental internal magnetic field measurements were taken at .2038 m downstream from the exit of the coil, at six different radial positions: r = -0.02514 m, -0.0129 m, -0.00003 m, 0.01916 m, 0.03807 m, and 0.6299 m. The sixth radial position is outside of the computational mesh, and was omitted for this analysis. Virtual $B_z$ probes were placed at the same z-coordinate in the numerical model and at the absolute value of the radial position. This is valid since the model is axially symmetric. Two of these are shown in Figures 4.5 and 4.6. Plots of the other probe positions may be found in the appendix.

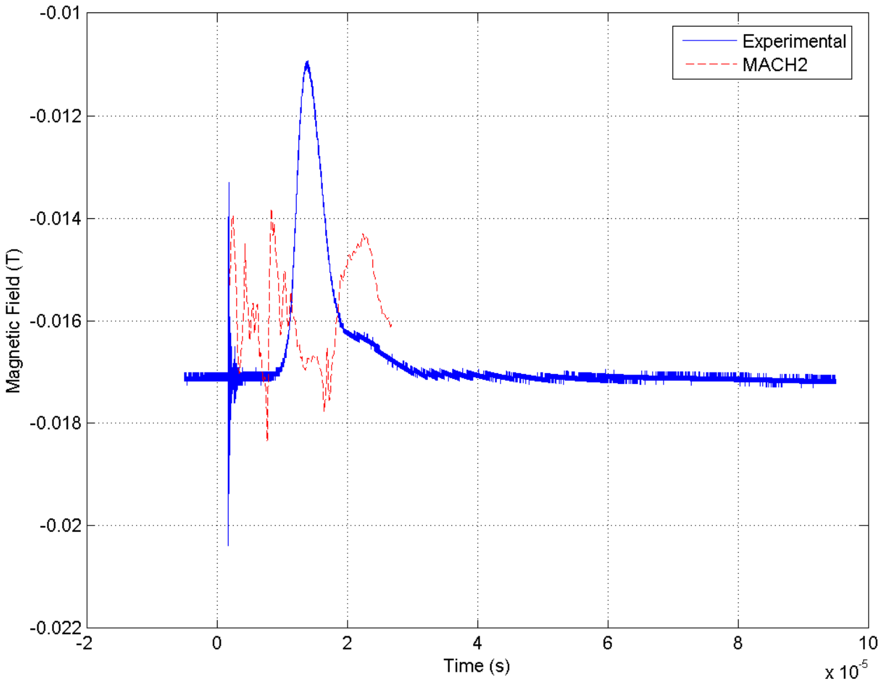

Figure 4.5 Internal Magnetic Field at r = 0.02514 m

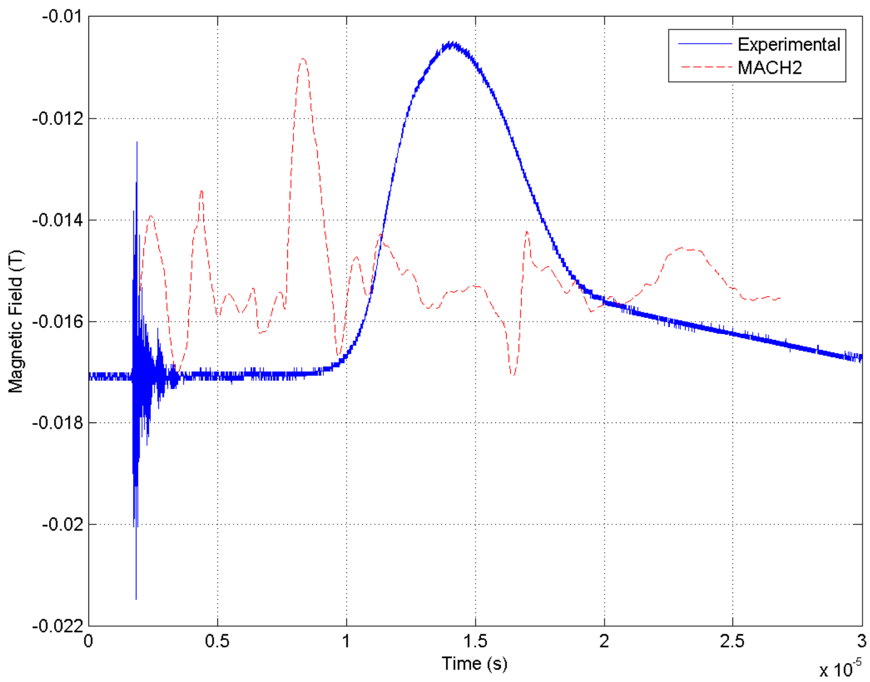

Figure 4.6 Internal Magnetic Field at r = 0.01916 m

These plots show that the downstream magnetic fields do not agree. This could be because of several reasons. The coupling between the plasma and the coil may not be modeled well in MACH2, possibly due to poor ionization. In the experiment, the plasma is preionized through a transient in the switch during initiation, which dies after the first half cycle. This is not reflected in the numerical model. Some cases using preionized slugs of gas were done to evaluate this theory.

The two preionized cases used slugs of gas inside of the coil. One was set at an initial temperature of 0.5 eV and the second was set at 2 eV. A comparison of the preionized and non-preionized cases with the experimental data is given in Figures 4.7 and 4.8. The preionized cases also show poor coupling between the plasma and the coil.

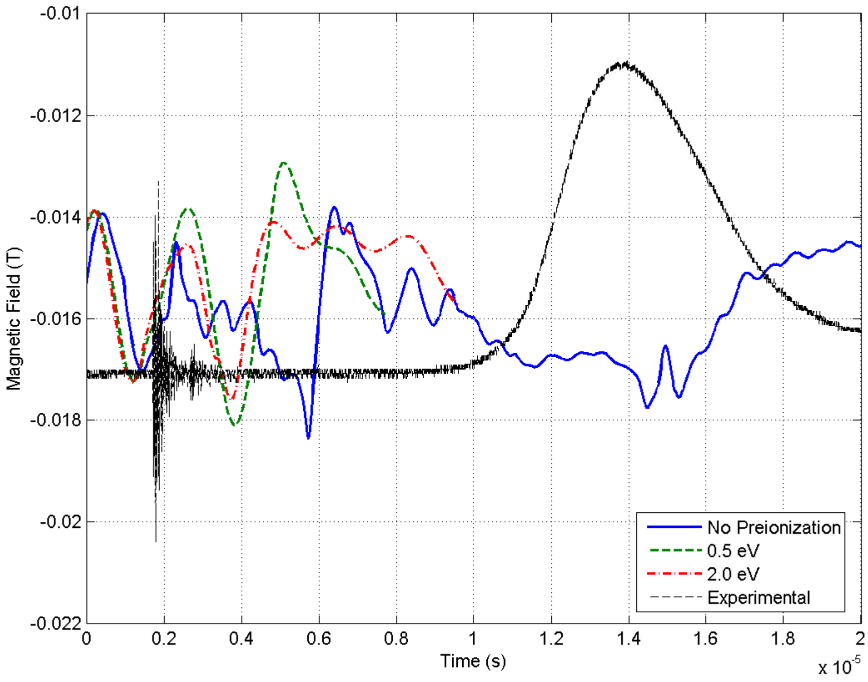

Figure 4.7 Comparison of Cases at r = 0.02514 m

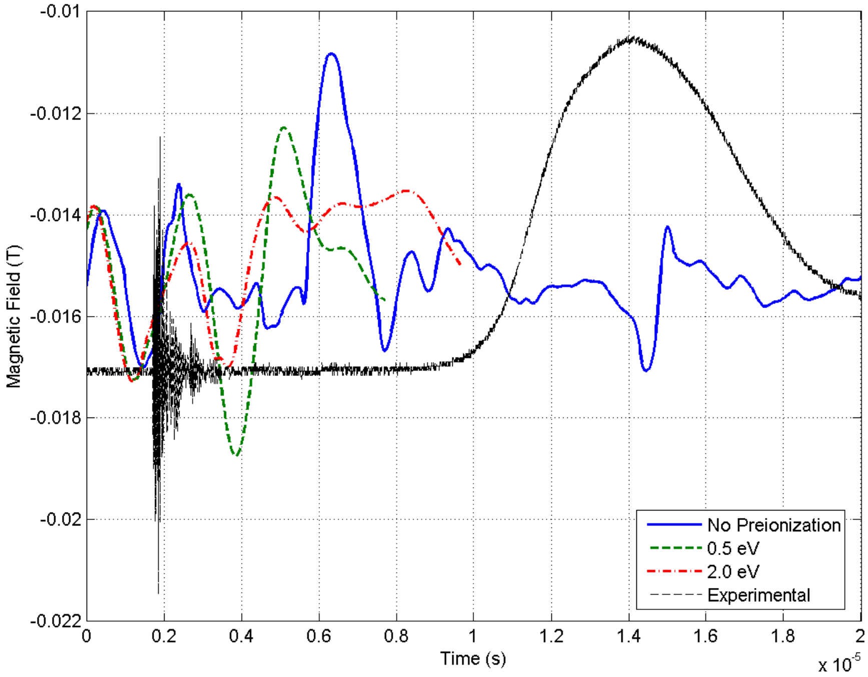

Figure 4.8 Comparison of Cases at r = 0.01916 m

The experimental data show that there is little residual field left in the plasmoid as it reaches this position downstream. This is supported by MACH2 using the Spitzer and Chodura resistivities with coefficients previously specified. Another quality that can be inferred from the numerical model is that several plasmoids are being formed. This is shown in both the cases where the gas was preionized and that which was not. One hypothesis is that in the experiment, these plasmoids coalesce into a more massive plasmoid, which will move more slowly than the individual plasmoids due to the increase in mass. This coalescence was not seen in the numerical model at this station downstream.

### 4.3.3 Interferometry Measurements

Interferometry measurements were taken at a z-position of 0.204m and radial positions from 0.0 ≤ r ≤ 0.111 m. Interferometry measures the line integrated electron density. This data are given in Figure 4.9.

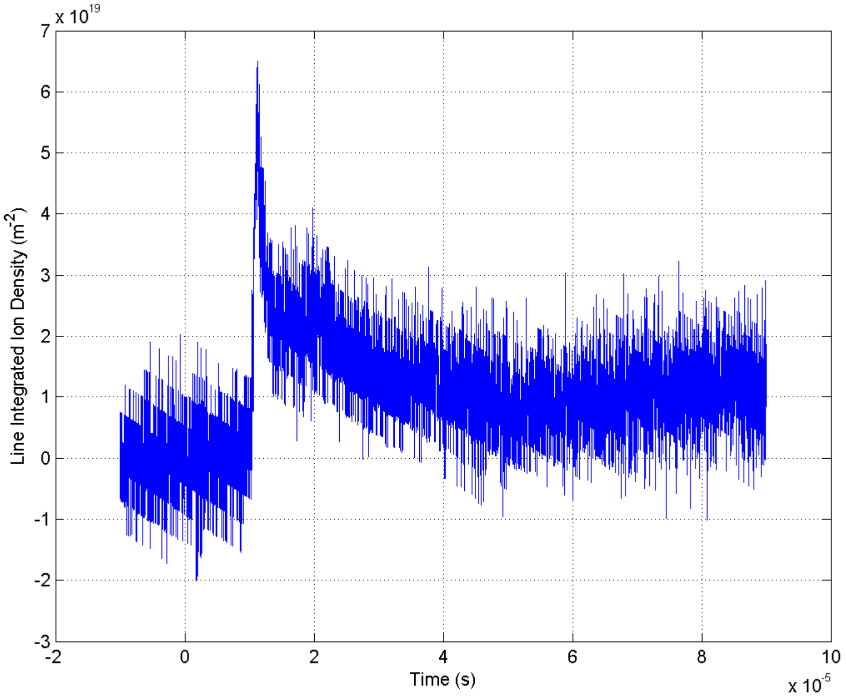

Figure 4.9 Experimental Line Integrated Density

An average line integrated density was also calculated from the numerical model, as shown in Figure 4.10. This density is close to the experimental data [3]. The preionized cases are shown in Figurea 4.11 and 4.12. These show a higher density than the experimental data. This is due to the slug of gas as an input, rather than the gas injection model. The magnitude of the line integrated density is the same for both preionized cases; however, the gas travels faster for the 2eV case than the 0.5 eV case. In summary, higher densities and velocities correspond to higher temperatures. Since the ionization fraction and plasma conductivity both increase with temperature, it can be surmised that PTX will operate more effectively as preionization is enhanced.

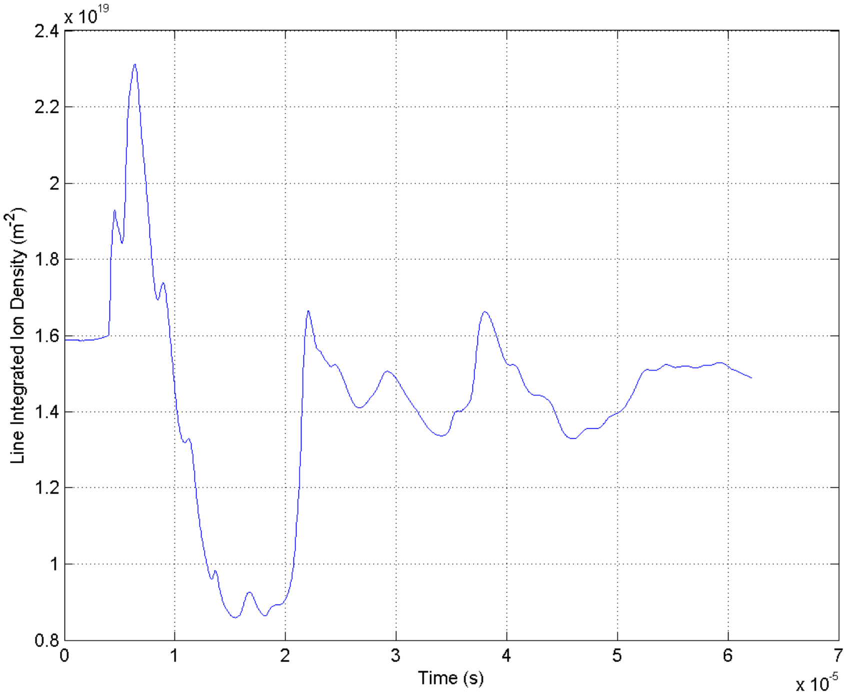

Figure 4.10  MACH2 Line Integrated Density, No Preionization

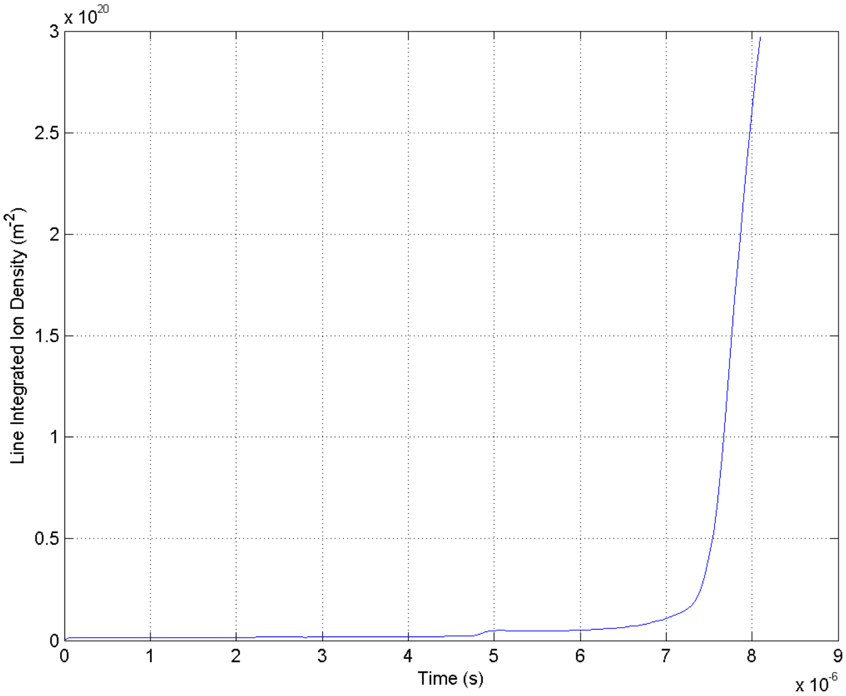

Figure 4.11 MACH2 Line Integrated Density, 0.5 eV Initial Temperature

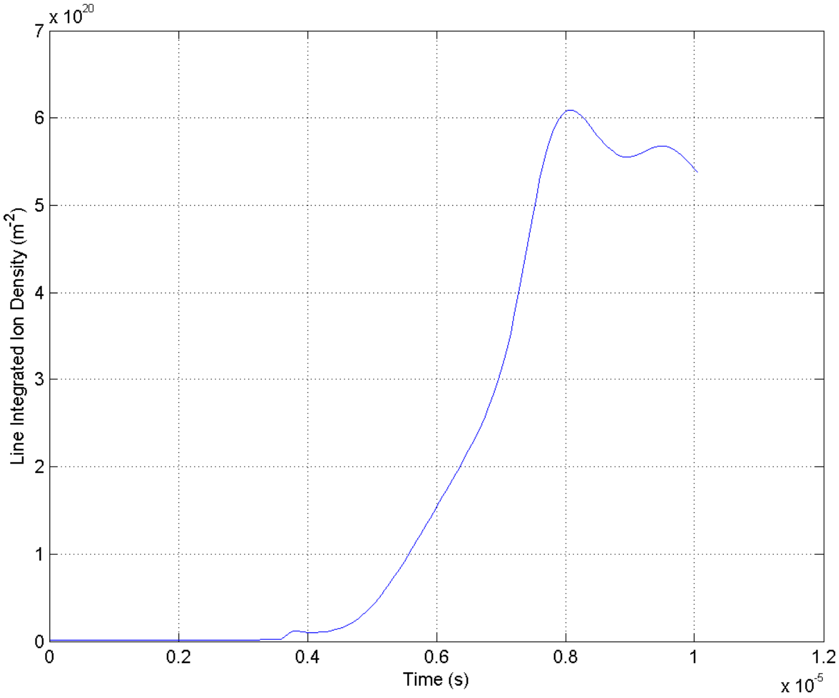

Figure 4.12 MACH2 Line Integrated Density, 2.0 eV Initial Temperature

### 4.3.4 Plasmoid Formation

Several plasmoids were seen in the numerical model. These plasmoids would form and quickly dissipate, as shown in Figures 4.13 through 4.15. The times called out in the plots represent the time after the coil has been fired, and the arrows represent the 2-dimensional magnetic field. In the figures, the plasmoids that formed dissipated quickly and did not translate downstream very far, as was seen in the experiment. Figure 4.14 shows two plasmoids being formed that seem to coalesce. The plasmoids in Figures 4.14 and 4.15 form around pockets of higher density than the surrounding fluids. This is consistent with detailed magnetic field measurements made in recent experiments [10].

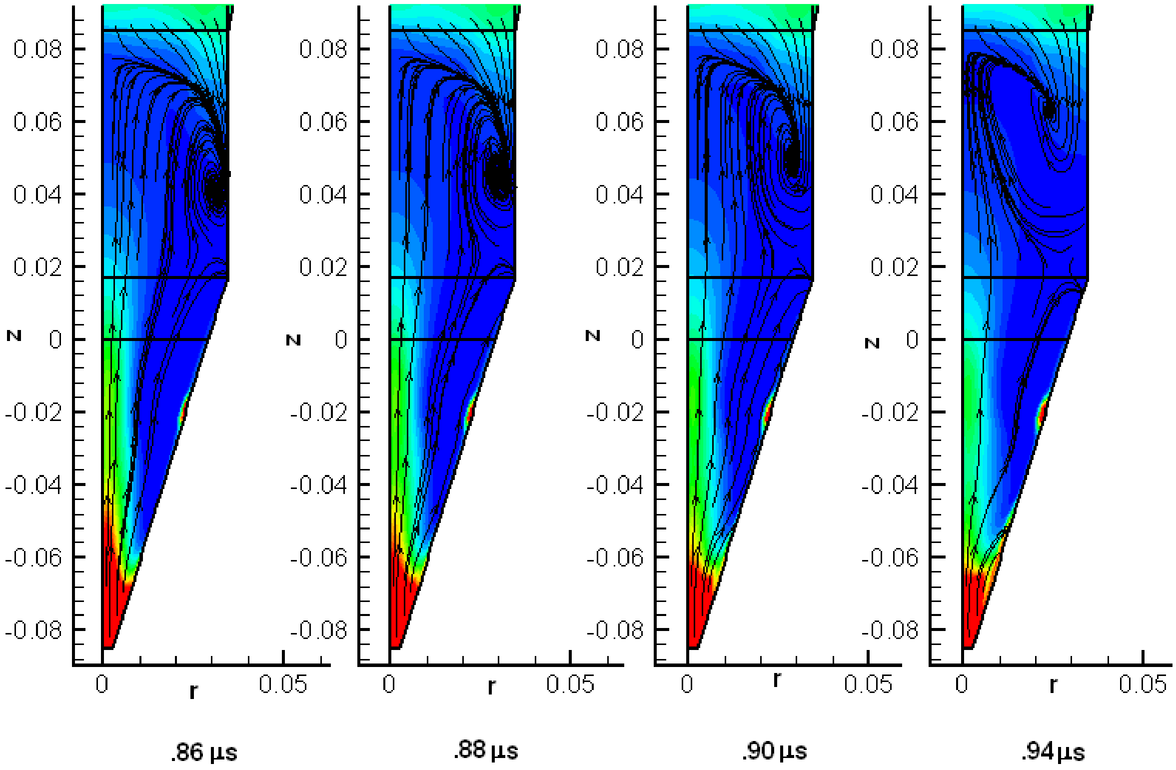

Figure 4.13 Plasmoid Formation, No Preionization, 0.86 µs to 0.94 µs After Coil Fires

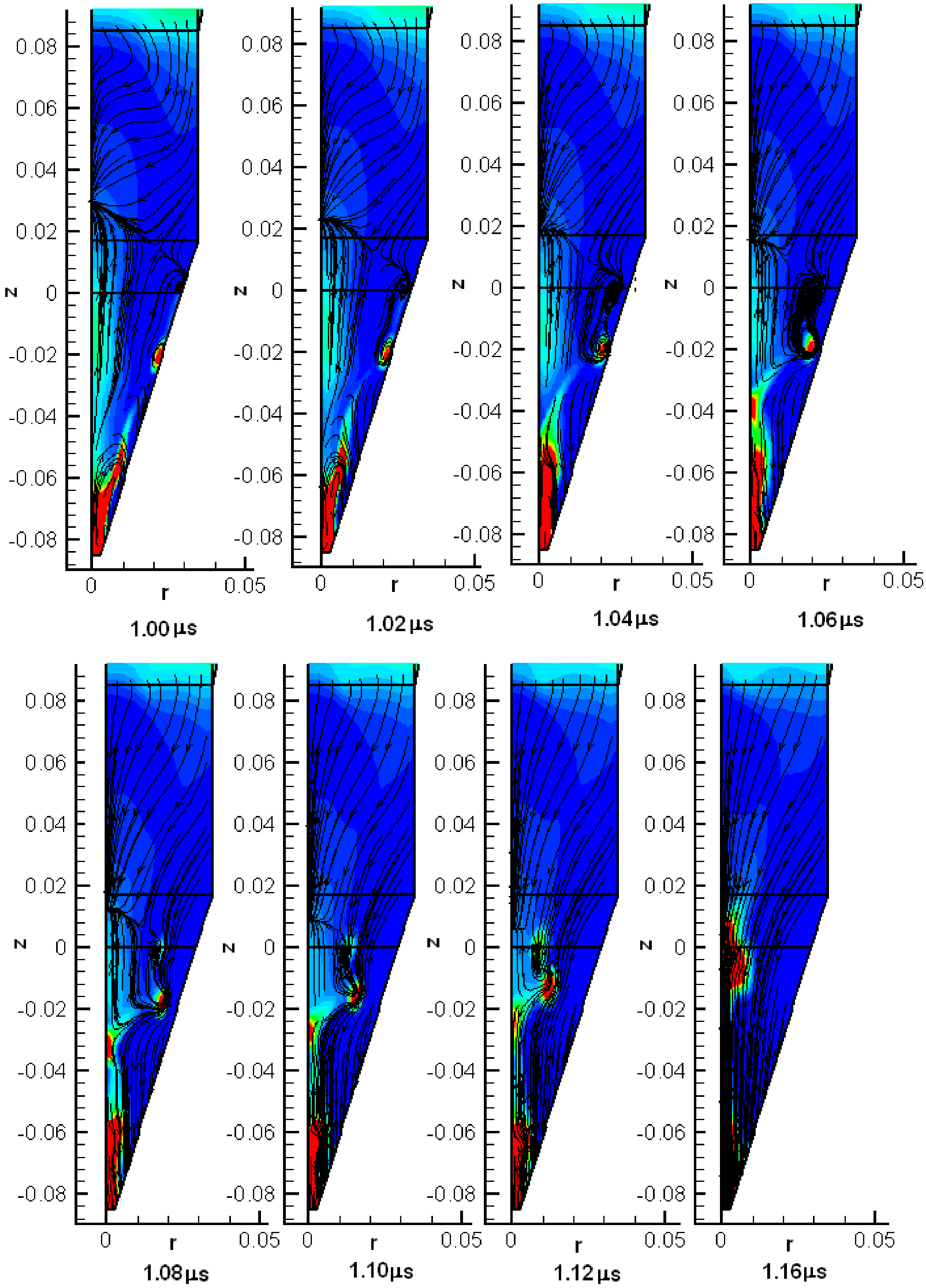

1.00 µs 1.02 µs 1.04 µs 1.06 µs

1.08 µs 1.10 µs 1.12 µs 1.16 µs

Figure 4.14 Plasmoid Formation, No Preionization, 1.00 µs to 1.16µs After Coil Fires

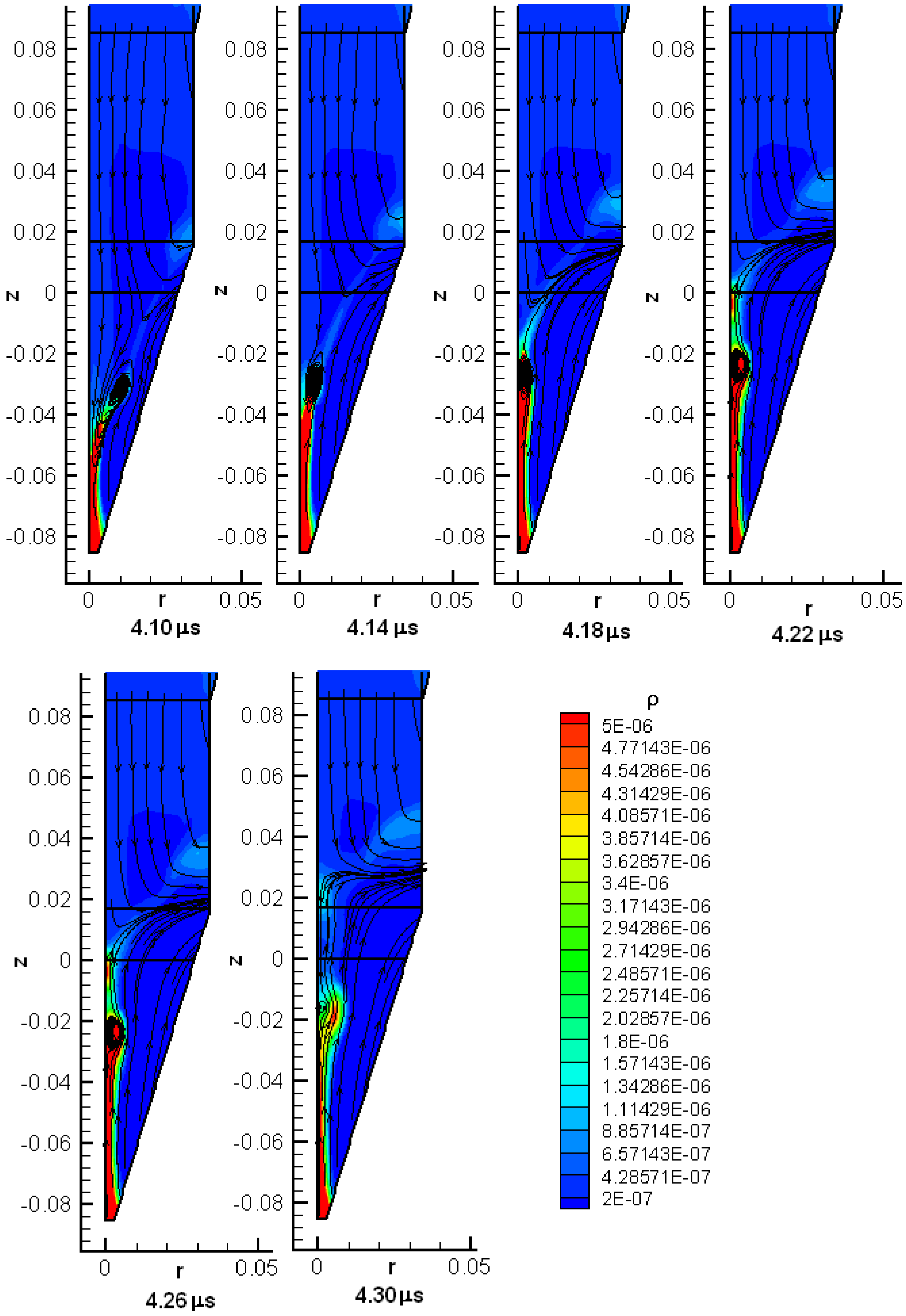

Figure 4.15 Plasmoid Formation, No Preionization, 4.10 μs to 4.30 μs After Coil Fires

When the gas is preionized before it goes into the coil, the plasmoids do remain for a longer period of time, but still dissipate before traveling downstream. The plots show that these may be impeded by a higher density downstream, blocking the translation of the plasmoids. Figures 4.16 and 4.17 show the plasmoid formation when preionized at 0.5 eV. Figures 4.18 and 4.19 show the formation when the gas is preionized at 2.0 eV. Again, the times represent the time after the coil fires, and the arrows are the magnetic field lines.

Unlike the non-preionized case, plasmoids are seen to form behind one which has already been formed (Figures 4.17 and 4.19) without coalescing.

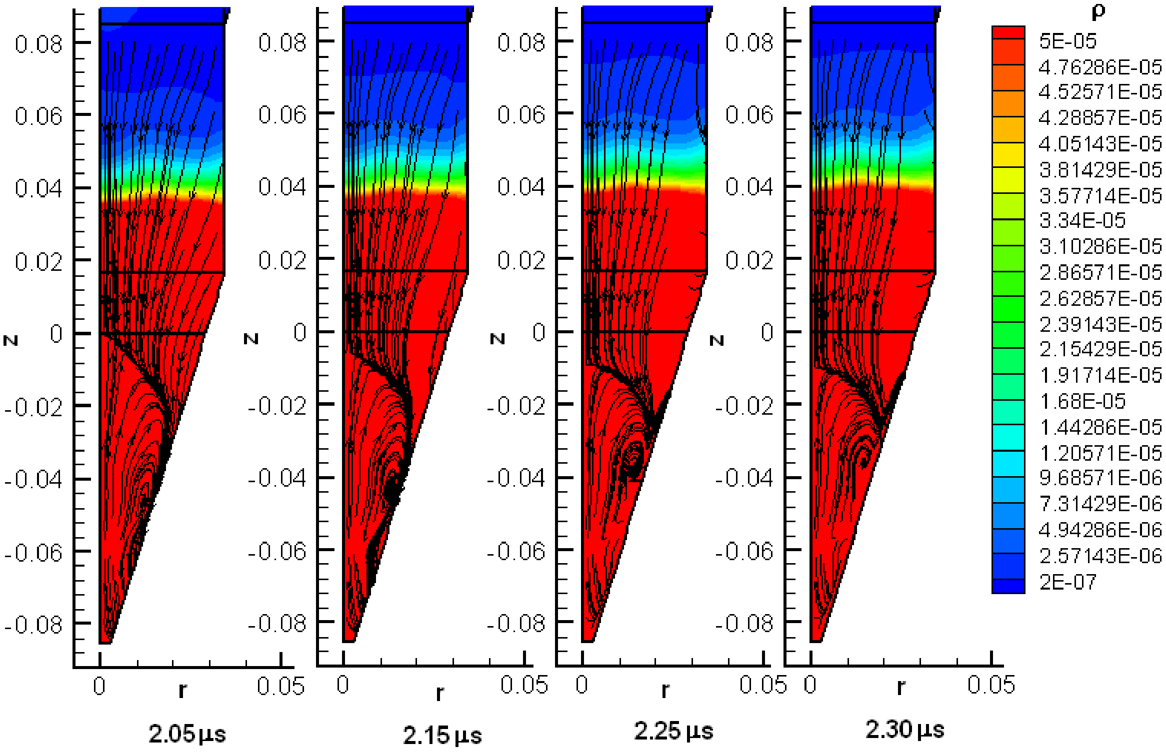

Figure 4.16 Plasmoid Formation, Preionized at 0.5eV, 2.05 μs to 2.30 μs After Coil Fires

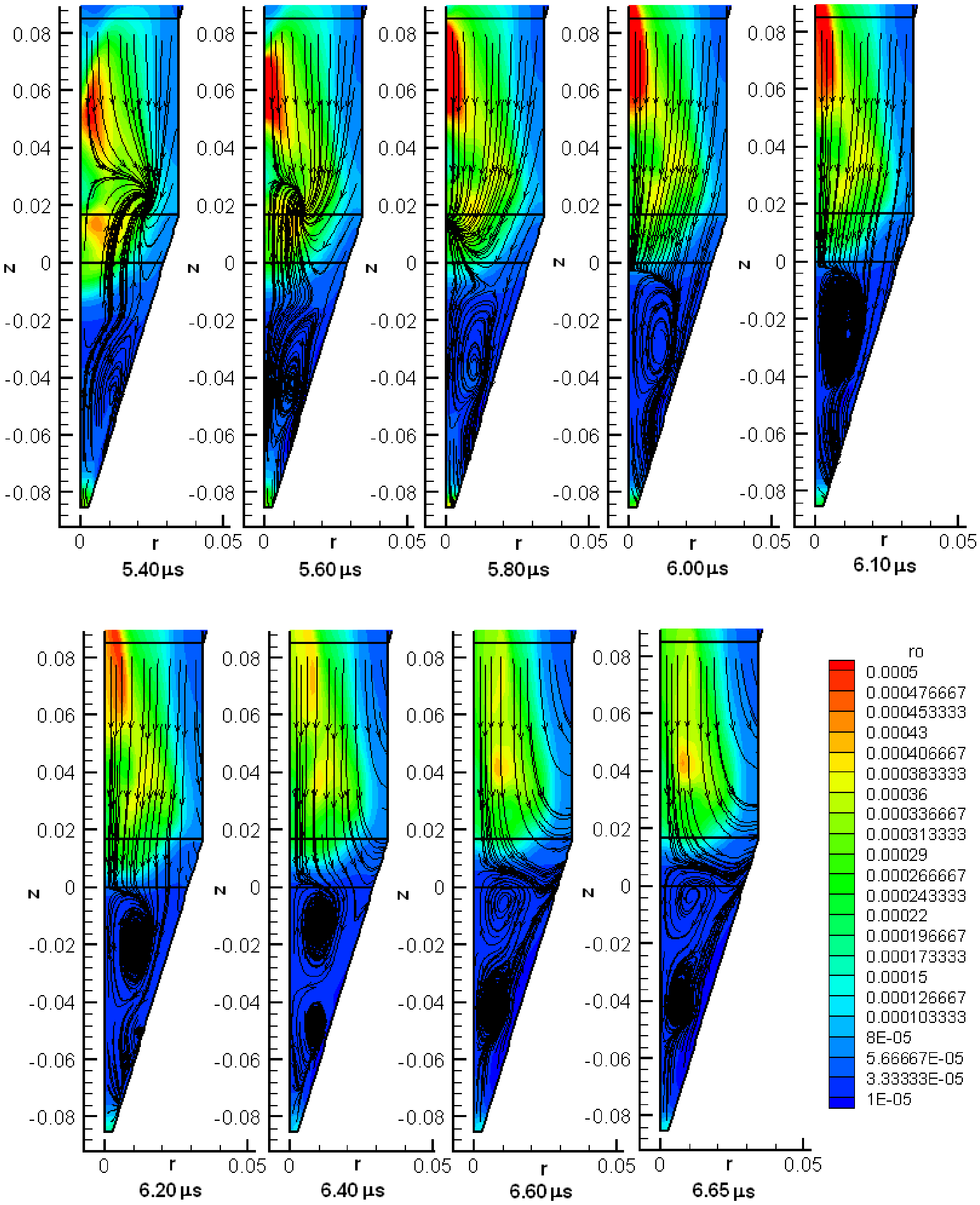

Figure 4.17 Plasmoid Formation, Preionization at 0.5 eV, 5.40 μs to 6.65 μs After Coil Fires

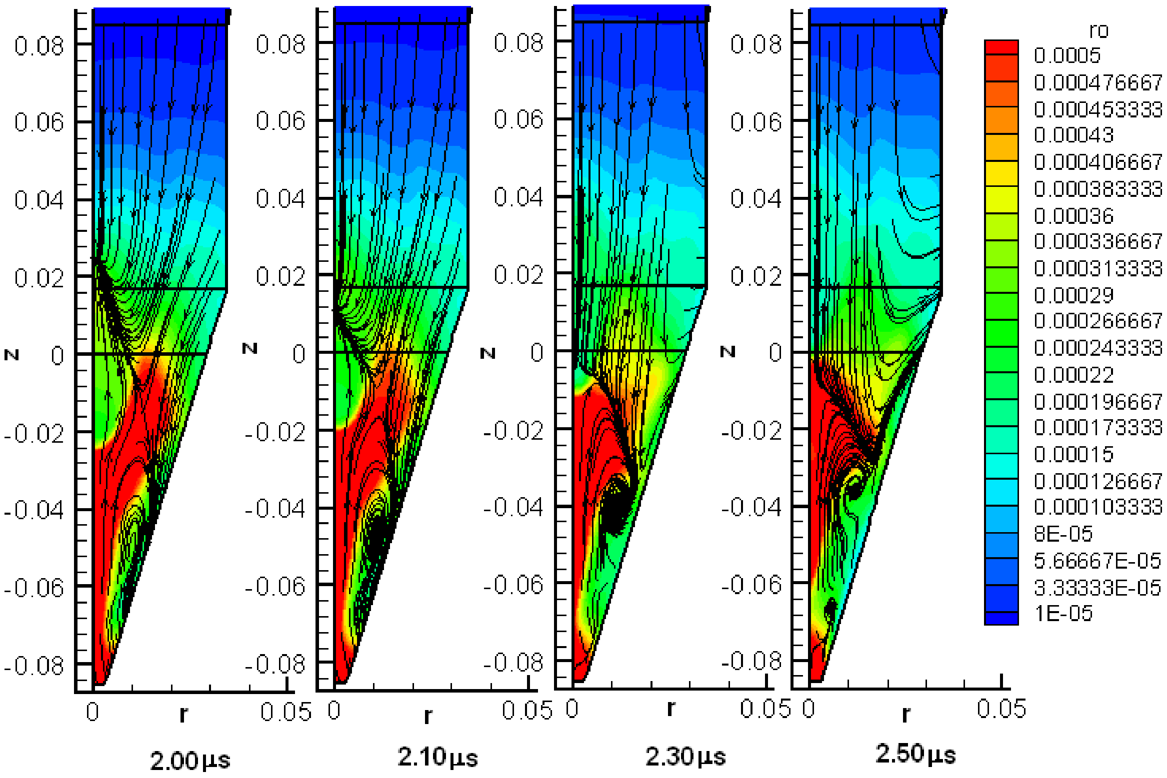

Figure 4.18 Plasmoid Formation, Preionization at 2.0 eV, 2.00µs to 2.50 µs After Coil Fires

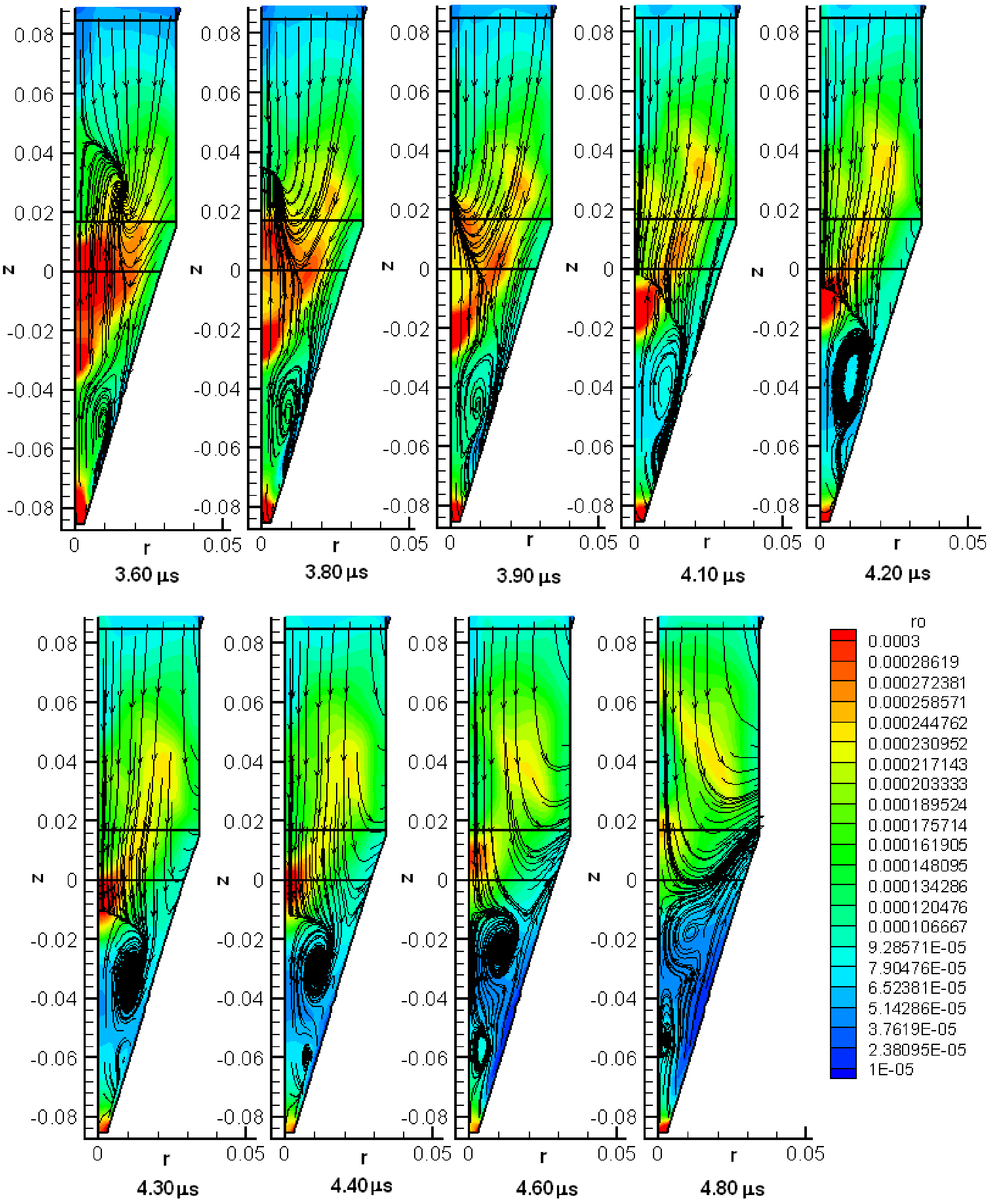

Figure 4.19 Plasmoid Formation, Preionization at 2.0 eV, 3.60 μs to 4.80 μs After Coil Fires

The numerical model does support some assessments of the experimental data including verification of plasmoid formation and that there is little or no residual field in the plasmoid downstream. No translation of the plasmoids is seen in the numerical model. Some improvements to the model need to be made to become more useful.

# CHAPTER V

# CONCLUSIONS AND FUTURE WORK

## 5.1 Conclusions

The plasmoid thruster is a pulsed inductive thruster that is potentially a good candidate for in-space propulsion. Several advantages to this type of thruster are its high specific impulse, the minimization of electrode erosion, and the absence of magnetic detachment problems.

A numerical model was developed to develop insights into the plasmoid thruster experiment. The important components of this model were the geometry, gas injection, circuit model, and resistivity models.

The geometry modeled was a 2-D axisymmetric representation of the PTX experiment from the entrance to the theta-pinch coil through the downstream vacuum chamber.

The gas injection model was based on experimental data for hydrogen with a plenum pressure of 10 psig. The pressure profile was set at the coil, and was allowed to propagate through the computational mesh for the time between the opening of the puff valve, and the firing of the coil.

The MACH2 RLC circuit model showed good agreement with the experimental data, with only a 7.6% difference in current measurement. The magnetic field generated by the coil at the outside edge of the computational mesh also agreed well with experimental data. Two of the three probes inside the coil measured a magnetic field within 1.5% of the experimental data. The third probe was 20% higher than the experimental data.

Internal, downstream magnetic field measurements from the numerical model do not match experimental data. The numerical model shows multiple spikes in the B-field, implying the formation of multiple plasmoids. PTX showed a single plasmoid passing the probe. This is likely due to poor knowledge of the actual initial conditions and perhaps the appropriate resistivity model. Two preionized cases were examined. While these cases showed little improvement in agreement with the experimental data, it was observed that increased initial ionization resulted in higher plasmoid velocities and densities.

The numerical model developed did show the formation of plasmoids in the coil. The plasmoids formed from the non-preionized case dissipated more quickly than those from the preionized cases. More plasmoids are formed with the preionized cases than without. These plasmoids were not seen to travel downstream, as was shown in the experiment, and these observations about formation were consistent with recent detailed magnetic field measurements.

## 5.2 Suggested Future Work

Further experimentation would be of use to better understand the plasmoid thruster. First, another variable needs to be measured in the gas injection, so the state can be identified, and a more accurate model produced. Intrusive magnetic field probes positioned radially inside the coil would be of use to better understand the magnetic field topology.

Numerically, the lack of transient in the signal can be tested by shutting off the circuit after a single plasmoid is formed.  This would mimic the preionization that was seen in the experiment.

# APPENDIX

## Internal Magnetic Field Probe Measurements

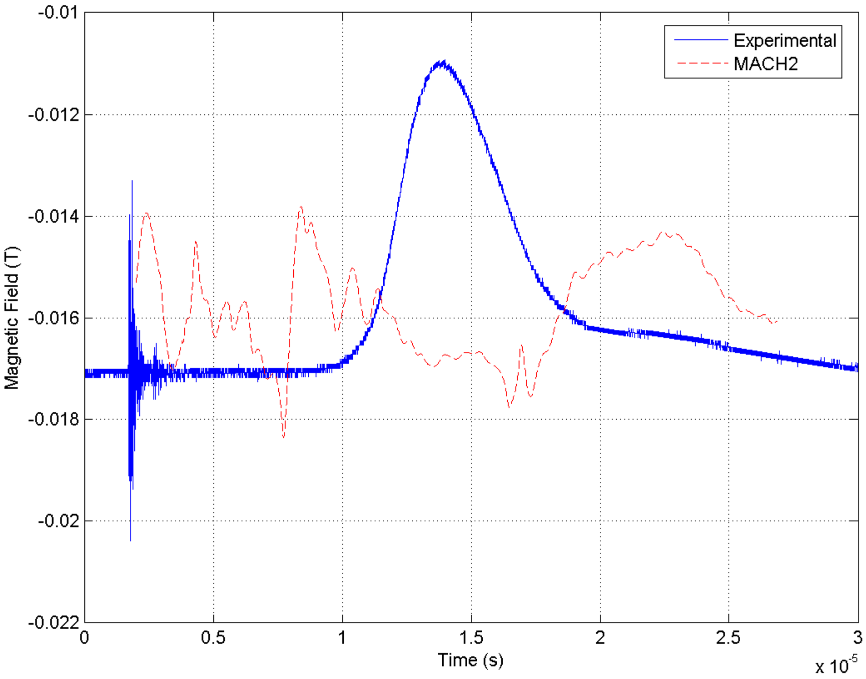

Figure A.1 Internal Magnetic Field at r = 0.02514 m, No Preionization

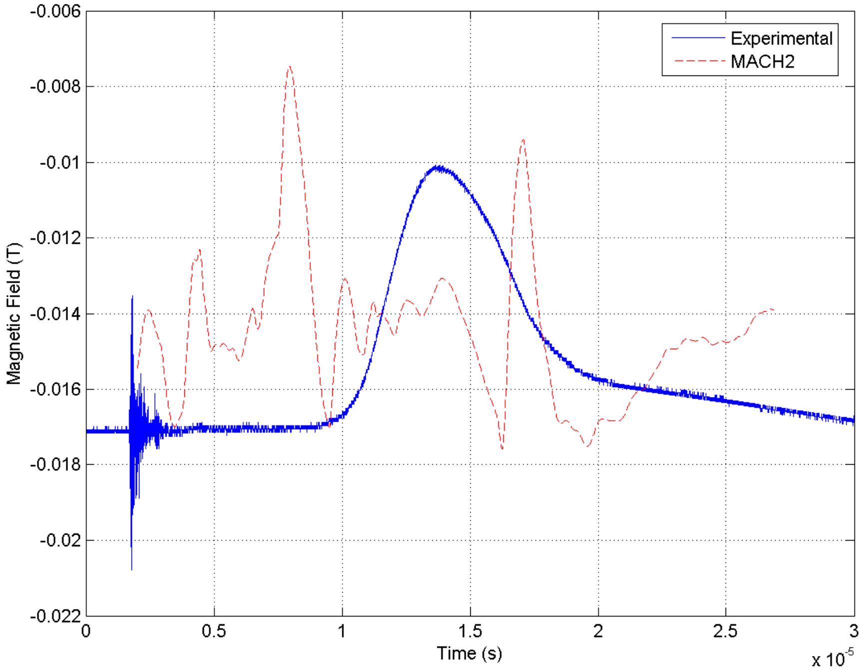

Figure A.2 Internal Magnetic Field at r = 0.01290 m, No Preionization

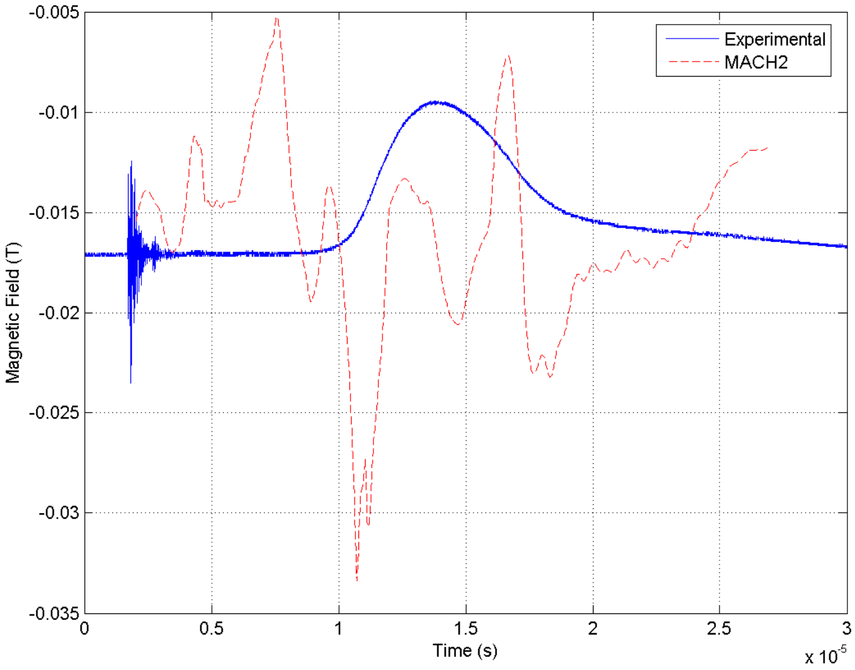

Figure A.3 Internal Magnetic Field at r = 0.00003 m, No Preionization

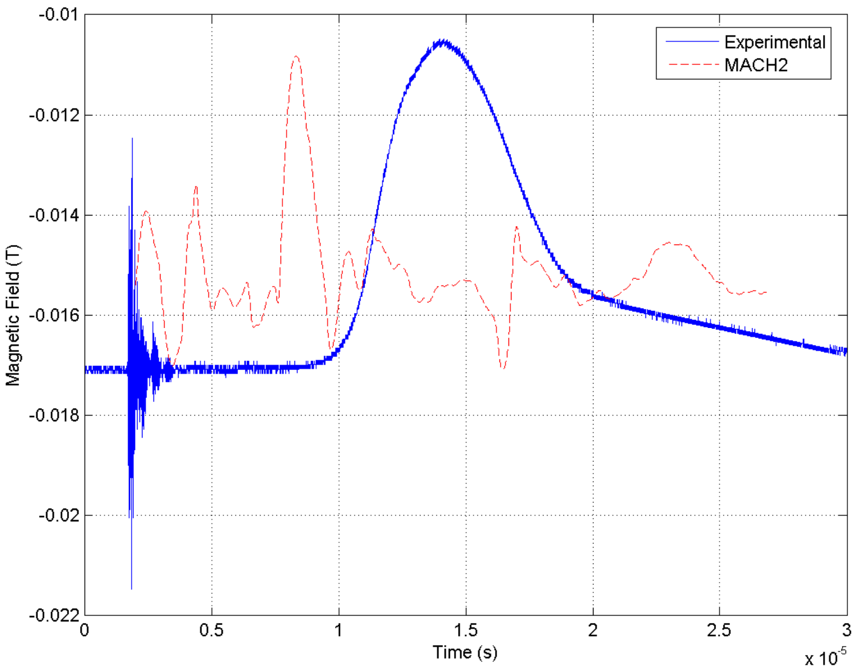

Figure A.4 Internal Magnetic Field at r = 0.01916 m, No Preionization

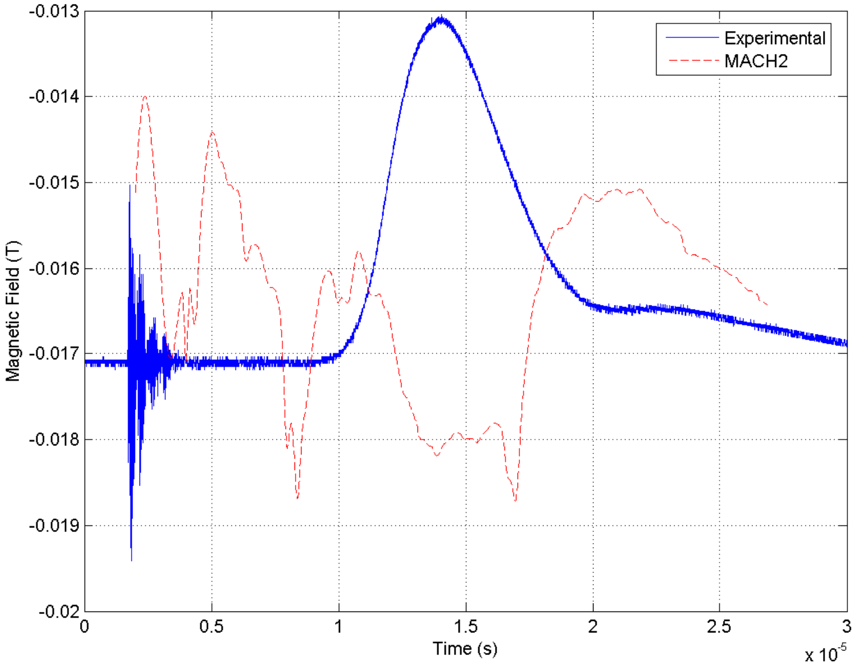

Figure A.5 Internal Magnetic Field at r = 0.01916 m, No Preionization

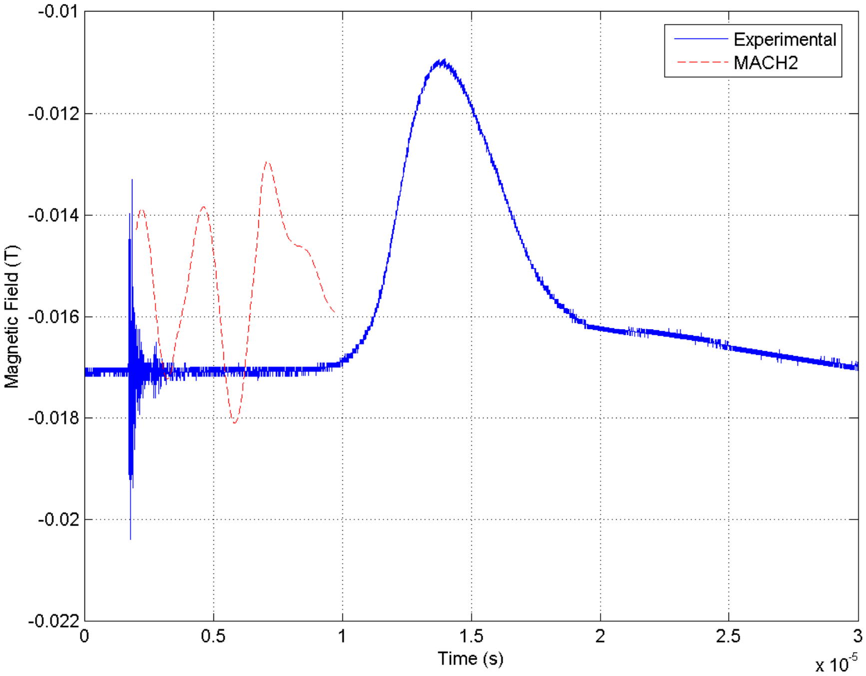

Figure A.6  Internal Magnetic Field at r = 0.02514 m, 0.5 eV Initial Temperature

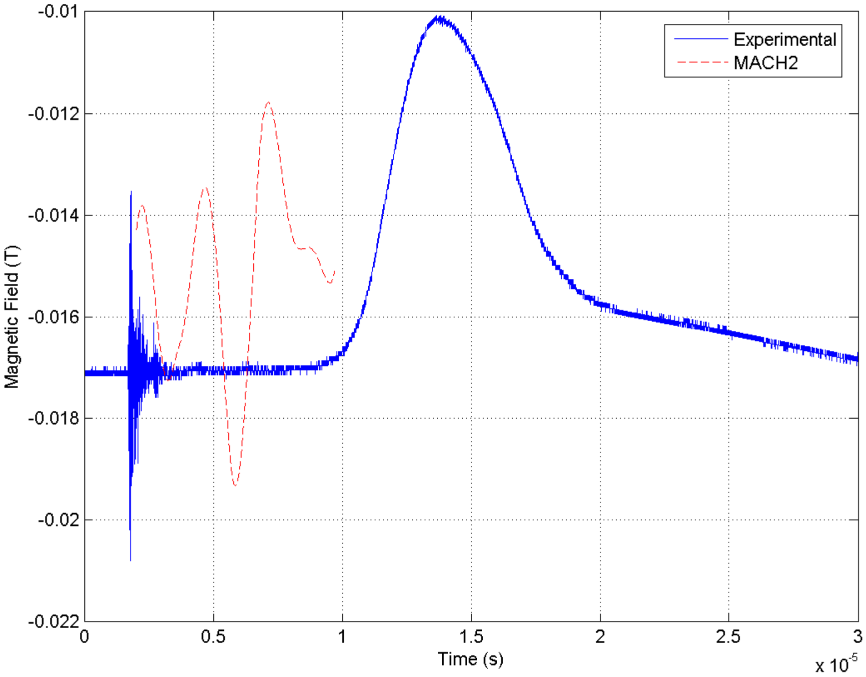

Figure A.7 Internal Magnetic Field at r = 0.01290 m, 0.5 eV Initial Temperature

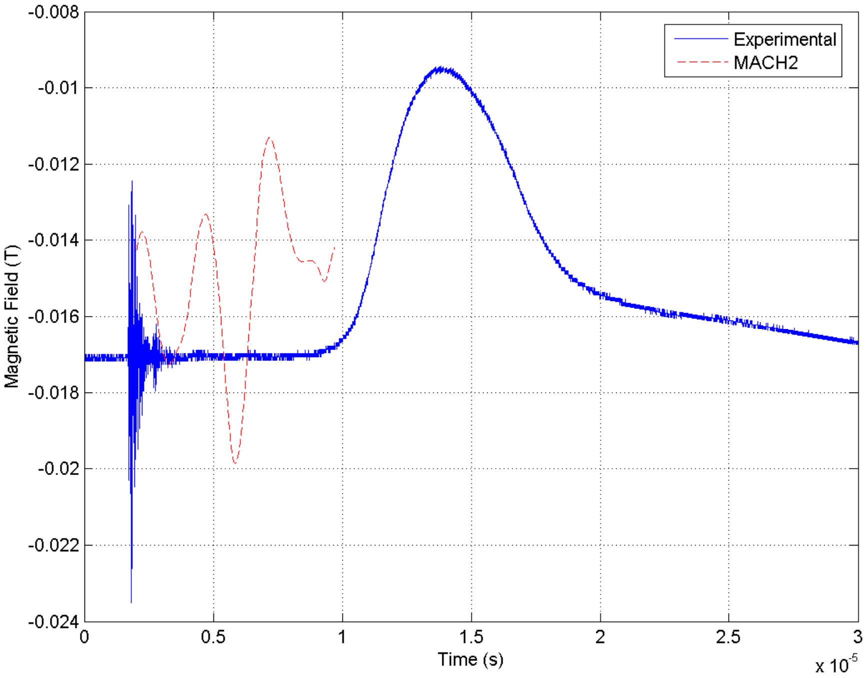

Figure A.8 Internal Magnetic Field at r = 0.00003 m, 0.5 eV Initial Temperature

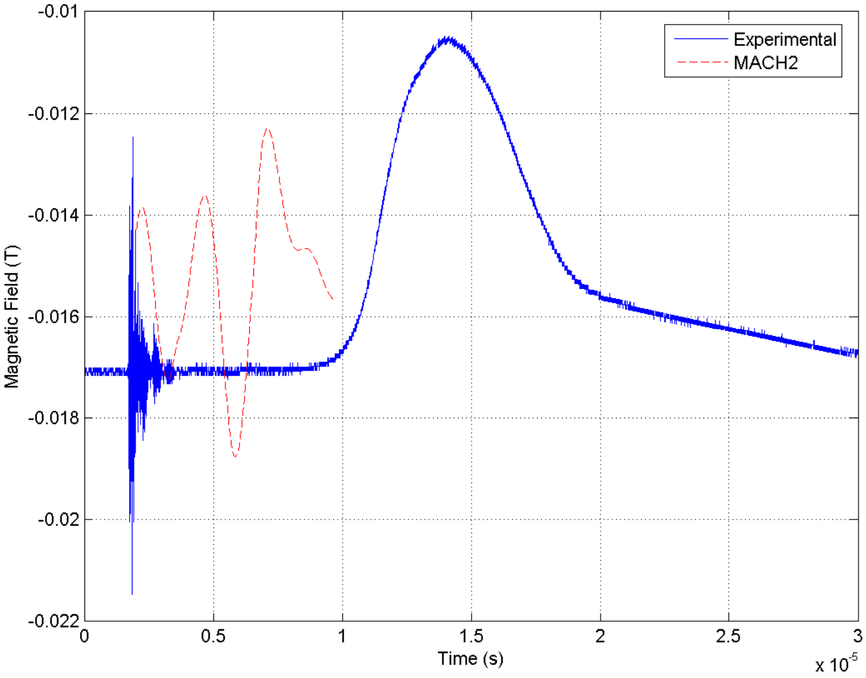

Figure A.9 Internal Magnetic Field at r = 0.01916 m, 0.5 eV Initial Temperature

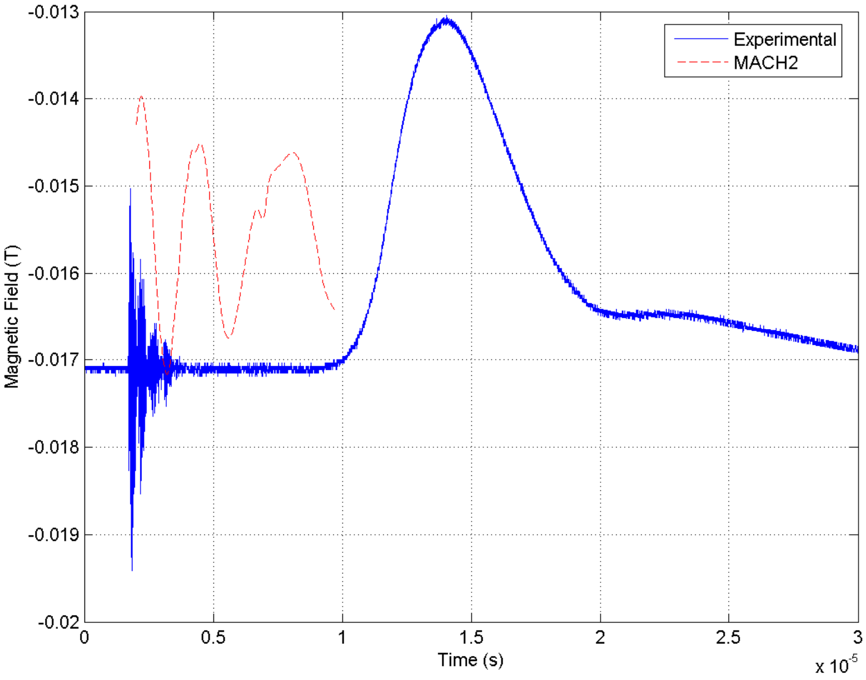

Figure A.10 Internal Magnetic Field at r = 0.03807 m, 0.5 eV Initial Temperature

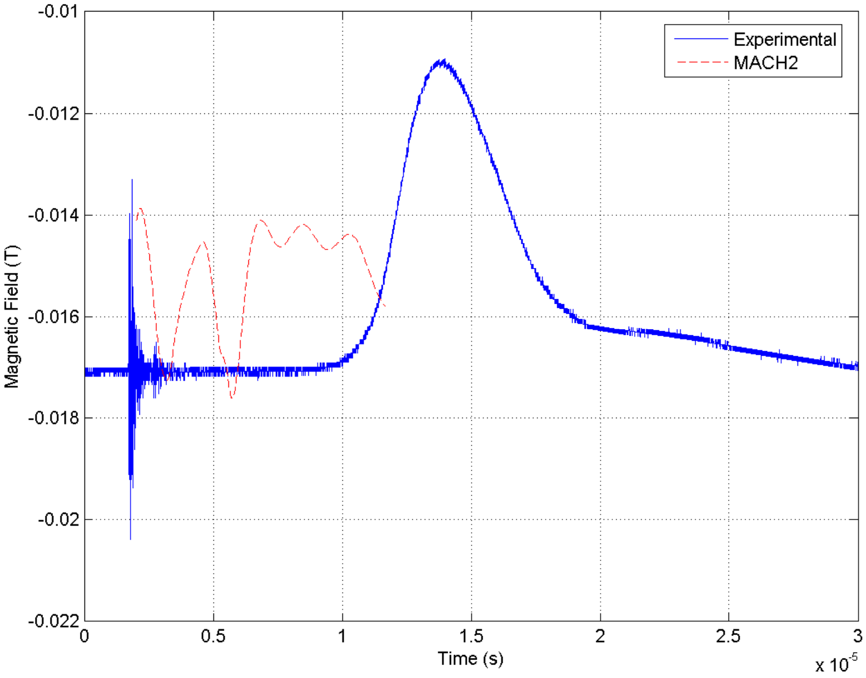

Figure A.11 Internal Magnetic Field at r = 0.02514 m, 2.0 eV Initial Temperature

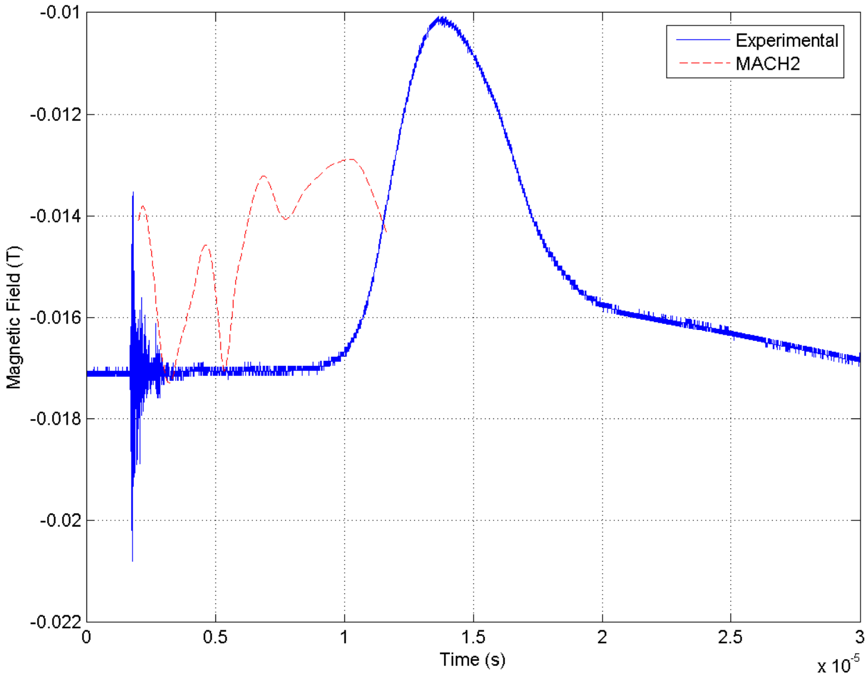

Figure A.12 Internal Magnetic Field at r = 0.01290 m, 2.0 eV Initial Temperature

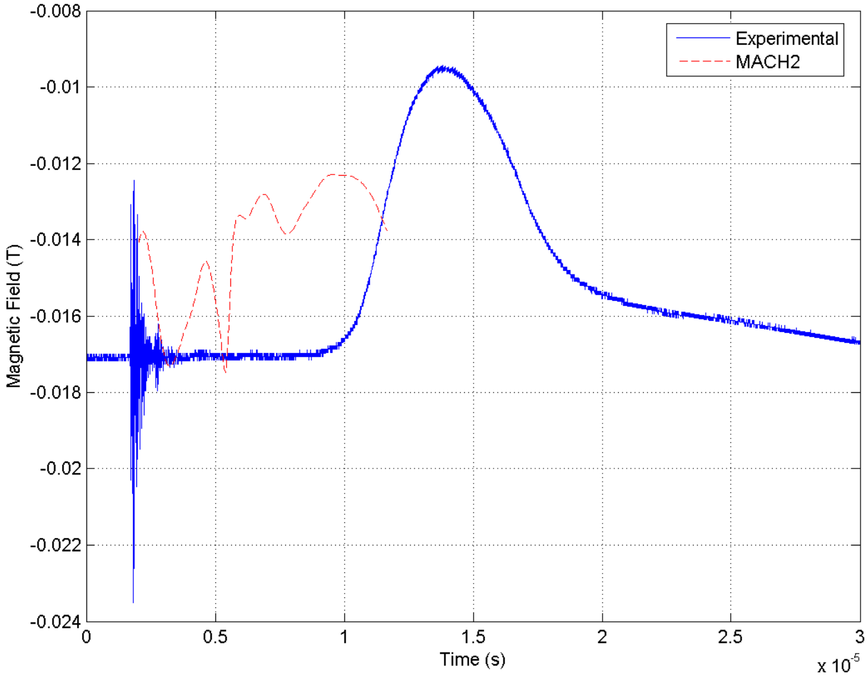

Figure A.13 Internal Magnetic Field at r = 0.00003 m, 2.0 eV Initial Temperature

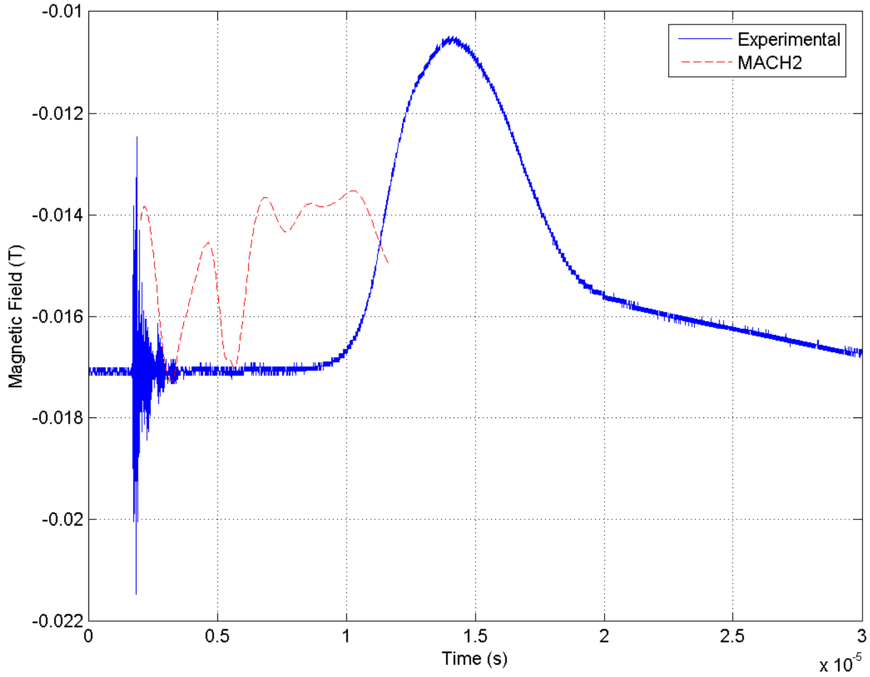

Figure A.14 Internal Magnetic Field at r = 0.01916 m, 2.0 eV Initial Temperature

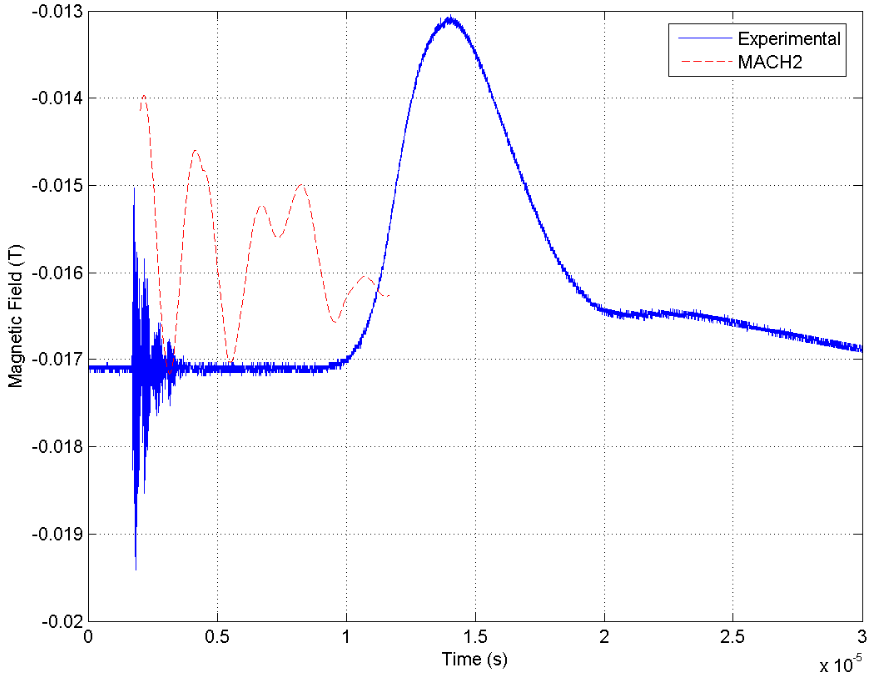

Figure A.15 Internal Magnetic Field at r = 0.03807 m, 2.0 eV Initial Temperature

# REFERENCES

[1] Jahn, R.G., *Physics of Electric Propulsion*. 1968, New York, NY: McGraw-Hill.

[2] Frisbee, R.H., *Advanced Space Propulsion for the 21st Century*. Journal of Propulsion and Power, 2003. **19**(6): p. 1129-1154.

.

[3] Koelfgen, S.J., *Magnetic Field and Quadruple Langmuir Probe Measurements in the Plume of the Plasmoid Thruster Experiment*, *in Mechanical and Aerospace Engineering*. 2005, University of Alabama in Huntsville: Huntsville, AL.

[4] Sutton, G.P., *Rocket Propulsion Elements, 7th Edition*. 2001, New York, NY: John Wiley & Sons.

[5] Cassibry, J.T., and Wu, S.T., *Comparison of Directly and Inductively Coupled Pulsed Electromagnetic Thrusters*. 36th AIAA Plasmadynamics and Lasers Conference, June 2005.

[6] Martin, A., and Eskridge, R., *Electrical Coupling Efficiency of Inductively Coupled Plasma Accelerators*. Journal of Physics D: Applied Physics, 2005. **38**: p. 4168-4179.

[7] Choueiri, E.Y., and Polzin, K.A., *Faraday Acceleration with Radio-Frequency Assisted Discharge*. Journal of Propulsion and Power, 2006. **22**(3): p. 611-619.

[8] Polzin, K.A., and Reneau, J.P., *Effect of Conductive Walls on Performance of a Pulsed Inductive Thruster*. IEEE Transactions on Plasma Science, 2009. 37: p. 359-363.

[9] Tuszewski, M., *Field Reversed Configurations*. Nuclear Fusion, 1988. **28**(11): p.2033-2093.

[10] Peterkin, R.E., and Frese, M.H., A *Reference Manual – Second Edition*. 2000, Air Force Research Laboratory: Philips Research Site.

[11] Chen, F.F., *Plasma Physics and Controlled Fusion*. 1984, New York, NY: Plenum Press.

[12] Milroy, R.D., and Slough, J.T, *Poloidal Flux Loss and Axial Dynamics During the Formation of a Field Reversed Configuration*. Physics of Fluids, 1987. **30**(11): p. 3566 – 3573.